ANL-87-53

Development of Nuclear Magnetic Resonance (NMR) Imaging Technology for Advanced Ceramics

by W. A. Ellingson, J. L. Ackerman, L. Garrido, P. S. Wong, and S. Gronemeyer

Materials and Components Technology Division
Materials and Components Technology Division
Materials and Components Technology Division

Argonne National Laboratory, Argonne, Illinois 60439
operated by The University of Chicago
for the United States Department of Energy under Contract W-31-109-Eng-38

This report has been reproduced from the best available copy.

Available from the
National Technical Information Service
NTIS Energy Distribution Center
P.O. Box 1300
Oak Ridge, TN 37831

Price: Printed Copy A03
Microfiche A01

Distribution Categories:
Heat Engines (UC-111) and
Coal-Based Instrumentation
(UC-115)

ANL--87-53

DE89 006400

ANL-87-53

ARGONNE NATIONAL LABORATORY
9700 South Cass Avenue
Argonne, Illinois 60439

DEVELOPMENT OF NUCLEAR MAGNETIC RESONANCE (NMR) IMAGING TECHNOLOGY FOR ADVANCED CERAMICS

by

W. A. Ellingson, J. L. Ackerman*, L. Garrido*, P. S. Wong,
and S. Gronemeyer**

Materials and Components Technology Division

November 1988

Prepared for the U.S. Department of Energy, Office of Fossil Energy, Advanced Research and Technology Development Fossil Energy Materials Program (FWP 49640) and the U.S. Department of Energy, Assistant Secretary for Conservation and Renewable Energy, Office of Transportation Systems, as part of the Ceramic Technology for Advanced Heat Engines Project of the Advanced Materials Development Program (Contract ACK-85234).

*NMR Facility, Massachusetts General Hospital/Harvard Medical School, Boston, MA.
**Siemens Medical Systems, St. Louis, MO.

LEGIBILITY NOTICE

A major purpose of the Technical Information Center is to provide the broadest dissemination possible of information contained in DOE's Research and Development Reports to business, industry, the academic community, and federal, state and local governments.

Although a small portion of this report is not reproducible, it is being made available to expedite the availability of information on the research discussed herein.

TABLE OF CONTENTS

LIST OF FIGURES

LIST OF FIGURES (continued)

LIST OF TABLES

DEVELOPMENT OF NUCLEAR MAGNETIC RESONANCE (NMR) IMAGING TECHNOLOGY FOR ADVANCED CERAMICS

by

W. A. Ellingson, J. L. Ackerman, L. Garrido, P. S. Wong, and S. Gronemeyer

ABSTRACT

The distribution of organic binder/plasticizers (B/Ps) used in injection molding of structural ceramics is important because nonuniformity, and the resulting nonuniform porosity distribution after burnout of the B/Ps (also known as dewaxing), can cause nonuniform densification. Also, residual B/P left after dewaxing can cause local degradation of mechanical properties. Proton nuclear magnetic resonance (NMR) imaging is a chemically sensitive, nondestructive, noninvasive technique which is becoming well-established in the medical community. To date, however, little work has been done to adapt this technique to solid state applications such as imaging the distributions of organic B/Ps and porosity in green-state ceramics.

In the work described in this report, we have explored both solid-state NMR imaging to map the distribution of B/Ps in cold-pressed ceramic parts and solution NMR to image the open, i.e., surface-connected porosity in dewaxed parts. (Knowledge of the distribution of this porosity also gives us an idea of how uniform the density of the final part will be.) The ability to detect B/Ps was initially evaluated on a state-of-the-art 1.5-T medical imager (Siemens Magnetom™) with T_1-weighted imaging techniques and a 10-cm standard eye coil. However, this system did not provide adequate image resolution. One problem is that at room temperature the waxy ("soft-solid") B/Ps have spin-spin relaxation times (T_2s) of ~1 msec using spin-echo, phase-encoding techniques. Short T_2s imply long data acquisition times. We solved this problem by designing a special NMR probe for a 2-T, small-bore (~15 cm) superconducting magnet system. The special NMR probe, designed and built with field gradients of ~10 gauss/cm, has the ability to image material with $T_2 < 2$ msec by means of spin-echo phase-encoding techniques. Si_3N_4, SiC, and Al_2O_3 specimens, up to 25 mm in diam and containing various concentrations of B/P (2.5-15.5 wt.%), were imaged with a spatial resolution of ~300 μm. Thus, we demonstrated that NMR imaging has the potential to map the distribution of organic B/Ps. The initial results show that a medical system may not be able to detect B/Ps unless elevated temperatures are used, whereas experimental small-bore systems with higher field gradients and shorter switching times detect B/P distribution quite well.

In order to image empty volumes (i.e., open porosity), a filler fluid that gives a good NMR signal must be used as a marker. The filler fluid selected after extensive experimentation was benzene (which has a proton molarity of 67.3 M) doped with paramagnetic chromium acetylacetonate, $Cr(CH_3COCH_2COCH_3)_3$, at 10.3 or 20.6 mM. The filler fluid was introduced into the sample via vacuum impregnation. The fractional porosity, as measured by the detected NMR signal, is taken to be a fraction of pure benzene. This technique was experimentally verified on a set of Al_2O_3 specimens made at the ALCOA Research Center.

I. INTRODUCTION

The processing of high-performance structural ceramics planned for use in advanced heat engines requires much more understanding than has been achieved to date. Indeed, processing science has received the highest priority in a recent Congressional analysis of advanced ceramics technology.[1] The needed effort includes the development of practical in-process nondestructive evaluation (NDE) inspection methods in order to identify problems at the earliest possible stages in the process.

One ceramic processing method that holds the potential for efficient large-scale production is injection molding. In the injection molding process, the distribution of organic binders/plasticizers (B/Ps), the degree of dewaxing (i.e, completeness of removal of the organics), and the distribution of open (i.e., surface-connected) porosity left by the removal of the organics are important because all of these affect local densification rates and hence mechanical properties. Indeed, as indicated in Table 1, poor disstribution of organic B/P has been identified as a potential cause of several types of injection molding defects. Cost-effective NDE methods to measure the distribution of the organic, the degree of dewaxing, and the distribution of the open porosity left after dewaxing would greatly aid the development of injection molding technology, and of ceramics processing in general.

Nuclear magnetic resonance (NMR) imaging (also called magnetic resonance imaging) is a chemically sensitive, noncontacting, and nondestructive imaging technique which has been routinely used in chemistry, physics, and biology for over 35 years. In these areas, its main applications are in determining chemical composition, molecular or crystal structure, and molecular dynamics.[3,4] The use of NMR to produce tomographic images of objects was reported in 1973.[5] The development of NMR imaging for medical diagnosis is now proceeding at a furious pace. However, efforts to apply NMR imaging in the materials sciences have begun only recently.[6-8] NMR imaging clearly holds potential for aiding in the development of ceramics processing. It is a particularly promising technique for investigating the spatial distribution of organic B/Ps. In addition, the amount and spatial distribution of porosity can be measured by introducing suitable filler fluids that contain nuclei from which an NMR signal can be obtained. Since NMR is noncontacting, it could be used on delicate green-state and partially densified ceramics without damage to the material.

Table 1. Injection Molding Defects and Causes[2]

Type of Defect	Causes
Incomplete part	Improper feed material Poor tool design Improper material and/or tool temperature Inadequate tool lubrication
Large pores	Entrapped air Improper material flow and consolidation during injection Agglomerates Large pockets of organic B/P due to incomplete mixing
Knit lines	Improper tool design or feed material Incorrect temperatures
Cracks	Sticking during removal from tool Improper tool design Improper extraction of B/P

In the work reported here, we have studied the potential of NMR imaging to tomographically map the distribution of the organic B/P in cold-pressed ceramic parts and the distribution of the open porosity left after dewaxing. NMR imaging was selected for evaluation because it seemed to hold potential for application to ceramic materials. Emphasis on injection-molded ceramics was chosen for the following reasons in addition to those noted above: (1) a reasonably high loading (~14-17 wt.%) of organic B/P is used in the process and thus there exists the potential for a reasonably large signal from the hydrogen protons in the organics, and (2) the very long burnout times associated with the B/P removal process provide a clear economic justification for gaining detailed knowledge of the distribution of the organic (i.e., the high cost of B/P removal should only be incurred for parts with uniform B/P distribution).

Prior to the present project, no work had been reported on the use of NMR imaging for ceramic applications. One problem with direct imaging of the organic B/P is that it is a "soft-solid." NMR measurements in solids generally require more specialized experimental techniques and place greater demands upon instrumentation than NMR measurements in fluids.[9,10] The absence of large-scale and isotropic molecular motion is the key element that complicates NMR measurement in solids (including "soft-solids"), for the following reasons:

(1) The spin-lattice relaxation time, T_1 (the characteristic time for the buildup of magnetic polarization of a nucleus), directly affects the rate at which data can be accumulated from successive acquisitions of NMR signals during the production of an image. Thus, the T_1 controls the total time that is necessary to acquire an image and the S/N ratio that is achieved per unit time. The lack of substantial molecular

motion in solids tends to lengthen T_1 considerably, especially for spins that are not part of an abundant reservoir (a collection of spins at relatively high concentration and strongly coupled to each other). Protons in typical organic solids form an abundant spin reservoir and can therefore relax by means of spin diffusion to rapidly relaxing T_1 "sinks" (e.g., paramagnetic centers or rapidly rotating methyl groups). Rare (chemically or isotopically dilute) spins of $I = 1/2$ do not possess any such mechanism and can have exceedingly long T_1s, although spins of $I > 1/2$ may relax by means of the quadrupolar interaction. Since protons are the most abundant nuclei in most B/Ps used in ceramics, they are the best candidates for NMR imaging, and so spin-lattice relaxation is not expected to be a major problem. For NMR imaging of ^{13}C or ^{29}S (^{13}C would be useful for silicon-containing ceramics), the exceedingly long T_1s[11] would have to be dealt with by special techniques.

(2) The spin-spin relaxation time, T_2, is the characteristic time for the decay of the transverse precessing magnetic moment that is detected as the NMR signal. This relaxation time affects the achievable spatial resolution and S/N ratio. Long T_2s are desirable, and are found in compounds which have minimal spin-spin coupling and which form nonviscous solutions. T_2 should be significantly greater than the echo time (TE) in order to avoid limiting spatial resolution and S/N ratio. Static direct dipole-dipole coupling produces linewidths ranging from a few kHz to tens of kHz. Since the size of a coupling is proportional to the magnetogyric ratio of each spin of a coupled pair and inversely proportional to the cube of their separation, couplings involving abundant protons tend to produce linewidths at the upper end of the scale and shortened T_2s on the order of tens of microseconds. This extreme shortening of T_2 is most severe for completely rigid proton-containing solids. In the case of Carbowax (polyethylene glycol, or PEG), polyvinyl alcohol, and similar waxy polymeric B/Ps, the small amount of molecular motion present creates T_2s on the order of hundreds of microseconds in length.

(3) The anisotropy of the chemical shift produces broad "powder pattern" lineshapes. Fortunately, this broadening interaction can be refocused with a 180° RF pulse that is normally used in the production of a spin echo.

These three factors conspire to produce a low S/N ratio per unit of data acquisition time, and large intrinsic spectral bandwidths, for solids. Large spectral bandwidths make imaging-plane selection difficult and degrade the spatial resolution of frequency-encoded dimensions.

With standard imaging equipment, such as that used for medical NMR imaging, the shortest TEs that can be obtained are in the range of 12-17 msec. Since the T_2s of polymeric B/Ps tend to be on the order of 1 msec or less, we expected that it would be essentially impossible to obtain images of the organic B/Ps with conventional room temperature NMR imaging techniques. This was confirmed by some of our experiments.[12] However, use of a special NMR probe and special pulsing sequences made it possible to image the B/P directly at room temperature.

To image the open porosity after removal of the B/P was a somewhat easier task since we could, in theory, fill the open pore spaces with a filler fluid and image the fluid itself. We could thus use solution NMR imaging, which poses fewer problems than solid-state NMR imaging. The filler fluid selected must, of course, be one that gives a good NMR signal. Desirable properties of the fluid include a high concentration of the isotope of interest (hydrogen protons are generally used because of their superior NMR sensitivity) and chemical compatibility with the sample (no chemical reaction, dissolution, or swelling). The latter property would allow removal of the filler fluid after NMR analysis to permit subsequent testing with other methods.

After hydrogen protons, the isotope with the next highest sensitivity is ^{19}F, with an intrinsic sensitivity 0.8 that of ^{1}H. The isotopic abundance of ^{19}F is 100%, so that all fluorine contributes to the NMR signal. Many fluorocarbons are chemically inert towards the materials found in green ceramics and have low viscosities and low interfacial and surface tensions. Despite their high cost and certain complications, they have been used effectively as NMR markers in biological systems.[13]

To avoid artifacts and anomalous signal intensity variations, the filler fluid must also exhibit a simple NMR spectrum, ideally containing a single sharp resonance line. Such a simple spectrum results from the absence of chemical shift differences and spin-spin (or J-) couplings within the molecule, and will be exhibited by a compound possessing a high degree of chemical symmetry (i.e., chemical and magnetic "equivalence" of nuclei). Examples of good candidates for filler fluids that satisfy this criterion are water, benzene, acetone, and dimethylsulfoxide for proton NMR, and hexafluorobenzene for fluorine NMR.

By means of paramagnetic "doping" (addition of paramagnetic substances), filler fluid T_1s may be conveniently shortened from their natural values (on the order of seconds) to about 100 msec. This shortened T_1 offers an order of magnitude reduction in the total imaging time and a similar increase in S/N ratio per unit time over undoped fluids.[14] Paramagnetic doping was successfully accomplished in the present work.

II. BASIC PRINCIPLES OF NMR IMAGING

It is not possible or appropriate to give a comprehensive review of NMR imaging in this report. However, some background is necessary and will be presented ir this section.

Nuclear magnetic resonance imaging is, to a large degree, based on the same principles as NMR spectroscopy. Thus, in principle, one can image all NMR-active nuclei. Most efforts have focused on ^{1}H because of its superior NMR sensitivity. However, ^{31}Pn, ^{23}Na, and ^{19}F have also been studied.[4]

Solution NMR imaging has typically been pursued because of the inherent narrow resonance peaks. The spatial resolution achievable is dependent upon the width of the resonance peak, according to the basic relationship[14]

$$\Delta_x \gamma G > \delta\nu_{1/2} \quad , \qquad (1)$$

where Δ_x is the spatial resolution (mm), γ is the magnetogyric ratio (kHz/gauss), G is the strength of the applied magnetic field gradient (gauss/cm), and $\delta\nu_{1/2}$ is the full width at half-maximum or FWHM (1/Hz) for the spectrum of the species being imaged. Thus, for an active ^{1}H nucleus (γ = 4.2573 kHz/gauss), with $\delta\nu_{1/2}$ = 200 Hz, Δ_x can be calculated to be 0.1 mm if a 5-gauss/cm gradient is present. Clearly, for a nucleus with a broader spectrum (as in soft-solids), a higher field gradient is necessary to maintain the same spatial resolution. Because of the interest in imaging solids for materials research studies, a number of solid-state imaging schemes have recently been proposed.[15-19] Some of these have been used in the present work, and will be discussed after some attention is given to the physical aspects of the NMR imaging hardware.

A. Hardware

Figure 1 shows a schematic diagram of the basic components of an NMR imaging system. The main components are the superconducting magnet (which supplies the primary magnetic field, B_o), magnetic field gradient coils and gradient coil power supplies, RF transmitter and receiver coil with amplifier, gradient coil switching control, host digital computer, image display, and processor. In all subsequent discussions, the B_o field is taken to be coincident with the z-direction.

It is the presence of the gradient coils that differentiates NMR imaging from conventional NMR spectroscopy. Figure 2 is a simplified schematic of magnetic field gradients applied at two orthogonal directions in the absence of a z-axis field gradient. Since the resonant frequency of the active nucleus is dependent upon the magnetic field strength, the Fourier transform of the RF signal will yield a different spectrum for each direction of the magnetic field gradient. The direction of the field gradient is controlled by the host computer through the gradient coil control, as noted in Fig. 1.

Figure 3 shows several projections in Fourier space from which reconstructed tomographic images are made. Recalling Eq. (1), the full width of the spectrum of the received RF signal, $\Delta\omega(2\pi\Delta f)$, impacts the electronics of the receiving RF coil. First, the spectral bandwidth Δf can be related to the size of the specimen to be imaged as[9]

$$\Delta f \approx \gamma L G \quad , \tag{2}$$

where L (in cm) is the largest sample dimension to be imaged. Thus, for a 2-cm-diam specimen providing a ^{1}H signal in a 5-gauss/cm gradient, Δf = (4.2573)(2)(5) = 42.5 kHz. Clearly, the spectral bandwidth of the specimen cannot be broader than the spectral bandwidth of the RF probe. This condition is met if[9]

$$\Delta f_{probe} \approx f_o/3Q \quad , \tag{3}$$

where f_o is the Larmor frequency of the active nucleus and Q is the quality factor of the probe. It must be kept in mind that the sharper the tuned receiver, the greater the possible spatial resolution.

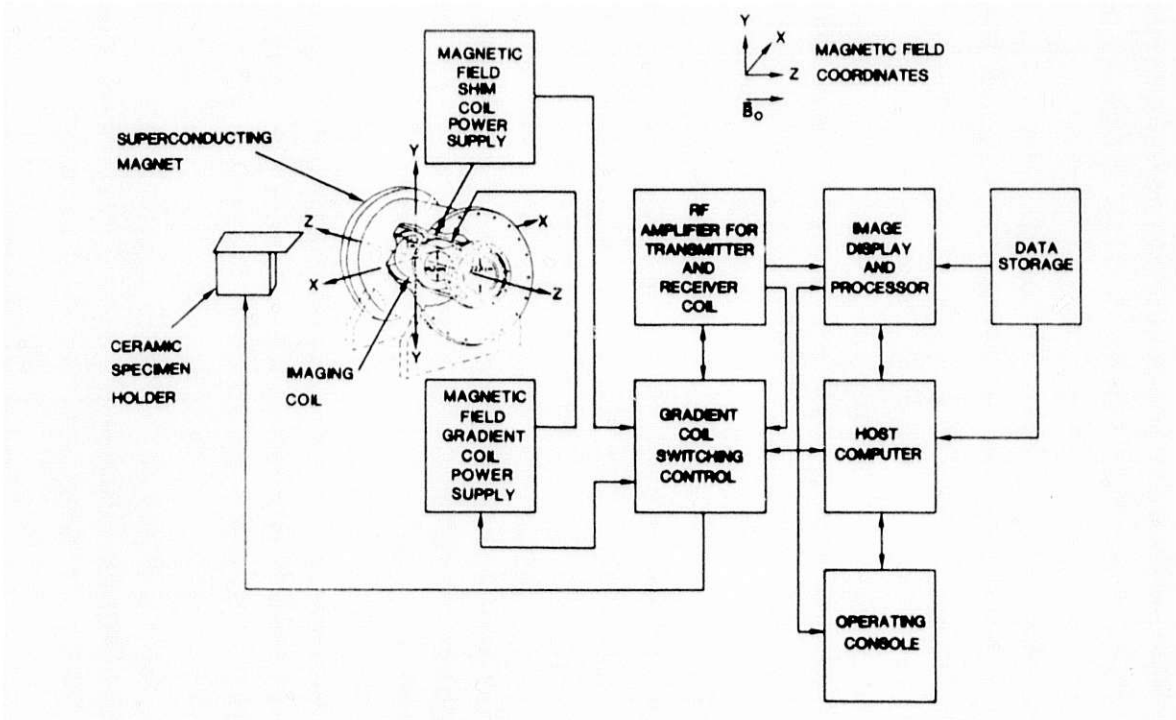

Fig. 1. Schematic Diagram of Basic Components of NMR Imaging System.

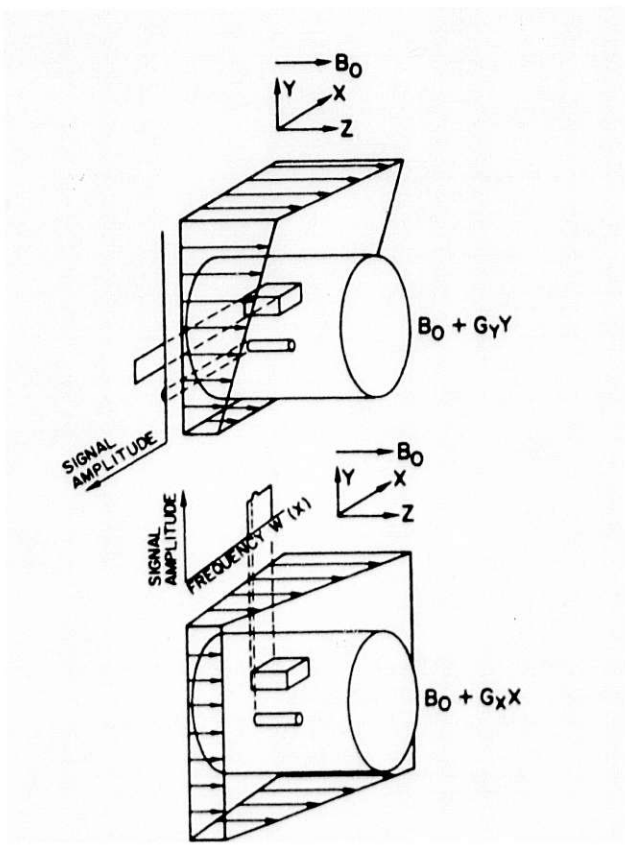

Fig. 2

Simplified Schematic Showing Magnetic Field Gradients Applied in the (a) z-y and (b) z-x Plane, with Two Resulting Projections after Transformation to Fourier Space.

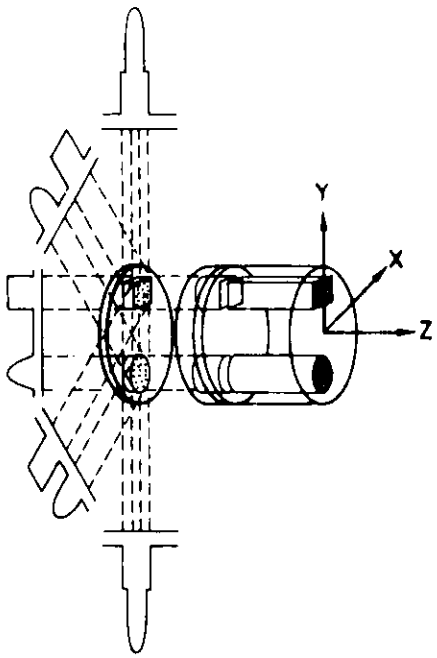

Fig. 3

Relationship Between a Three-Dimensional Object, Its Two-Dimensional Projections along the y-axis, and Four One-Dimensional Projections at 45° Intervals in the x-z Plane. The arrows indicate the gradient directions.

B. Spatial Encoding of Spin Densities

It was shown that the primary difference between NMR spectroscopy and NMR imaging is the intentional nonuniformity of the magnetic field. This nonuniformity is created by imposing a field gradient, usually made as linear as possible, over the sample. The gradients produce spatially dependent NMR frequencies that can be spatially encoded via signal processing and various reconstruction techniques such that a reconstructed tomographic image (i.e., a "slice") is generated. This approach is similar in many ways to that of X-ray computed tomographic (CT) imaging. However, in contrast to X-ray CT imaging, NMR imaging requires no mechanical motion to obtain different projections. Instead, the magnetic field gradients are rotated electronically and data are acquired at the respective field positions.

The three parameters that usually provide contrast in an NMR image are spin density (i.e., number of nuclei excited), spin relaxation (i.e., atomic level bonding), and chemical shift (i.e., shift in resonant frequency caused by local atomic structure). All of these are important in materials research studies, and will be briefly discussed in the following sections. In addition, although there are other spatial encoding methods, we will confine most of our discussion in this report to the two methods we have used to obtain images, i.e., back projection and phase encoding.

1. Back Projection

It was shown that NMR frequency is proportional to magnetic field strength. Thus, a magnetic field gradient can be used to spatially encode the resonant frequencies of the spins on the basis of spatial position relative to the magnetic field gradient. This can be shown mathematically by letting $S(\omega)$ be the frequency domain signal, $\rho(x,y)$ the two-dimensional spin density distribution, and G_x a magnetic field gradient along the x direction. One obtains[14]

$$S(\omega) = \int_{-\infty}^{\infty}\int \rho(x,y)\delta(\omega/\gamma G_x x)dxdy \qquad (4)$$

For a constant position on the x-axis, this can be rewritten as

$$S(\omega) = \int_{-\infty}^{\infty} \rho(\omega/\gamma G_x x)dy \quad . \qquad (5)$$

We recognize Eq. (5) as a line integral of the projection spin densities along the y axis. A projection along an arbitrary direction is obtained by acquiring data in the presence of an orthogonal gradient.

The reconstructed cross section computed by back-projection algorithms is a direct analogy to X-ray CT imaging, as shown in Fig. 4. To optimally sample an nxn two-dimensional image cross section, n projections are acquired, with each projection consisting of n rays, i.e., sample points. Acquisition times for spin-density back projection are typically on the order of a few minutes. This method of image reconstruction is quite susceptible to nonuniformities in magnetic field, since the spatial frequency is directly related to the magnetic field strength. However, since data can be acquired at a fixed position for a long period of time, the method has advantages for short-T_2 materials.

2. Phase Encoding

In order to reduce the effect of magnetic field nonuniformity, Fourier imaging methods[15-16] based on phase-encoding principles are commonly used. A common feature of all Fourier imaging methods is an evolution period during the pulse sequence when spatial information is phase encoded. Figure 5 shows a pulse sequence originally proposed by Kumar et al.[20] Improved versions of this pulse sequence have subsequently been introduced.[21]

For tomographic or three-dimensional imaging, x and y magnetic field gradients are applied during the signal evolution period. During this period, the time evolution of the nuclear spins is manifested in the initial phase of the detected signal (see Fig. 5). This initial phase shift relates the spatial positions of the spins along the x and y axes. To completely map over this plane, the evolution period is incremented by a fixed time delay with subsequent repetitions of the RF pulse sequence. Mapping along the z direction is usually achieved by frequency encoding the acquired data, i.e., a spin-density projection is obtained.

To produce a three-dimensional image consisting of n^3 pixels, n^2 image data must be acquired with different gradient evolution times. A three-dimensional Fourier transform over the three time increments subsequently produces the three-dimensional spin-density distribution, $\rho(x,y,z)$.

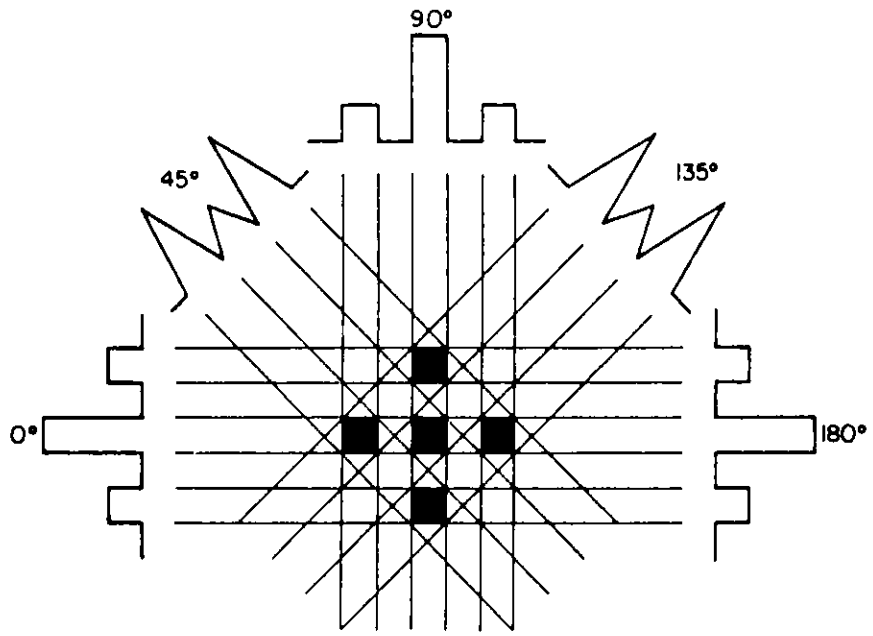

Fig. 4. Schematic Diagram of Spin-Density Projection Measurements. The black areas represent regions of homogeneous spin density. A projection of spin density is acquired at any angle by applying a magnetic field gradient orthogonal to the projection direction during signal acquisition. Shown are five projections with a 45° angular separation. The reconstructed image is produced by back projection. (After Rothwell et al., Ref. 14.)

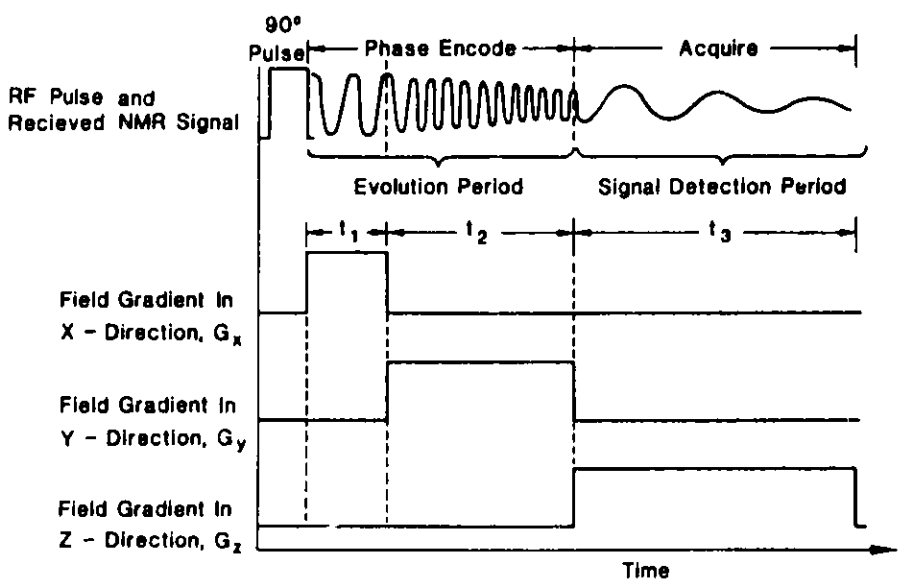

Fig. 5. Idealized Fourier Imaging Pulse Sequence as Proposed by Kumar et al.[20] Phase encoding is used to map spin density along the x and y axes. Note that gradient amplitudes rather than evolution times can also be incremented.

The basic RF and magnetic field gradient on-off sequence in Fig. 5 is generally modified on commercial medical imagers by using a fixed evolution time; with this technique, known as spin-warp imaging, the gradient amplitudes are time-sequentially incremented.[21]

3. Selective Irradiation

A third method of spin-density encoding which reduces local magnetic field inhomogeneities is a method called selective irradiation. In selective irradiation, the RF pulse is modulated so that only spins resonating at selected frequencies are nutated. If an RF waveform is modulated with a sin (bt)/t function, the result will be the generation of a narrow range of frequencies. If this narrow band of frequencies is selectively applied in the presence of a magnetic field gradient, a plane of spins perpendicular to the magnetic field gradient axis will be nutated. Note that in this case, slice position is controlled by the frequency of the RF excitation pulses and slice thickness is controlled by the modulated RF bandwidth.

In commercial medical imagers, planar image slices are selected in just this manner. Note that this procedure only defines the slice; it does not acquire data for image reconstruction. A common imaging approach combines selective-irradiation slice selection with spatial encoding by phase-encoding methods. If a complete volumetric image is needed, the data can be acquired simultaneously in a time-efficient manner by interleaving data acquired from sequential slices during the normal spin relaxation delay. Such a multislice imaging approach uses system data acquisition time that is normally "wasted" in the repolarization step of conventional single-slice imaging.

Figure 6 schematically shows how selective RF irradiation combines to define a selected "line" (really a volume, since the bandwidth will excite over a finite dimension) in an object. If a z-axis uniform gradient is applied, the spin density along a selected x-axis line is spatially encoded through a spin-density projection as shown earlier. Two- or three-dimensional images are produced by scanning this well-defined "line" over the slice of interest. It should be noted that line scanning techniques of this type are, however, inherently limited by poor S/N ratios.

It should be noted that important differences can exist between instrumentation for medical imaging and that which is optimally suited for the more general field of nonbiological imaging. These differences arise because of potentially different requirements for nonbiological imaging, e.g., shorter T_2 relaxation times, no health-related restriction on RF exposure of the sample, and reduced need for rapid imaging sequences. Because of the shorter T_2s found for many nonbiological samples, the more moderate gradient strengths found on many medical imagers may be inadequate. Another consequence of short T_2s is that shorter spin-echo times are needed for adequate S/N ratios. Thus, gradient switching times must be short -- of the order of 0.5 msec or less -- or techniques that do not rely on switching (e.g., projection reconstruction) must be used. This is the case for imaging soft-solids in ceramics, as described in a later section.

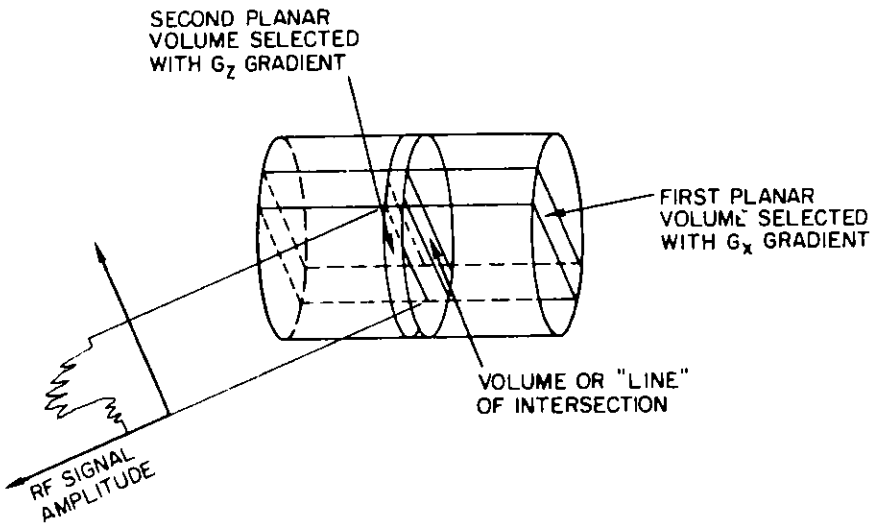

Fig. 6. Schematic Diagram Showing Slice and "Line" Selection by Selective Irradiation. The projection of the spin density along the line of intersection has been defined by the frequency of the RF pulse.

C. Relaxation Time and Chemical Shift Encoding

Other NMR parameters may also be used to obtain images by suitably modifying the basic pulse sequences. Relaxation times and chemical shift information, for example, can also be encoded.

T_1 relaxation times can be spatially encoded by initially saturating the spins with a specific train of RF pulses. A T_1-weighted image is produced by allowing the system to relax for a variable time, τ, prior to the spatial encoding step. Provided τ is shorter than the longest T_1 in the sample, those spins with short T_1 relaxation times will be preferentially enhanced in the resulting image.

In an analogous fashion, T_2-weighted images can be produced by means of a Carr-Purcell (C-P) sequence. In a C-P pulse train, a series of 180° RF pulses produces a series of spin echoes whose components decay with a rate T_2, as shown in Fig. 7. In such a fashion, a series of T_2-weighted spin-density projections can be obtained and an image reconstructed. However, in all relaxation-time-weighted images obtained in this manner, both spin density and relaxation time information is obtained. In order to separate these two factors, the data must be "fit," on a pixel-by-pixel basis, to appropriate theoretical expressions.[18]

Chemical-shift encoding is somewhat more difficult conceptually -- one must differentiate chemical-shift resonance offset effects from offsets due to gradients. One chemical-shift imaging method that has received wide attention is also based on Fourier imaging.[22,23] Field gradient and chemical shifts are separated in the manner illustrated in Fig. 8. The first in vivo application of chemical-shift encoding was reported in

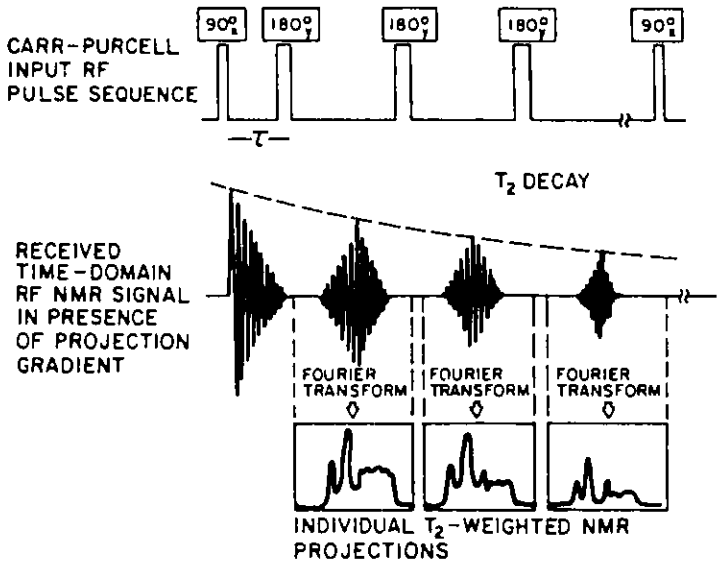

Fig. 7. T_2-weighted Images Are Commonly Produced by Combining a Carr-Purcell Sequence with Spatial Encoding. The example shown is for projection reconstruction. To be noted is that images produced from later echoes in the train preferentially map long-T_2 species. (After Rothwell et al., Ref. 14.)

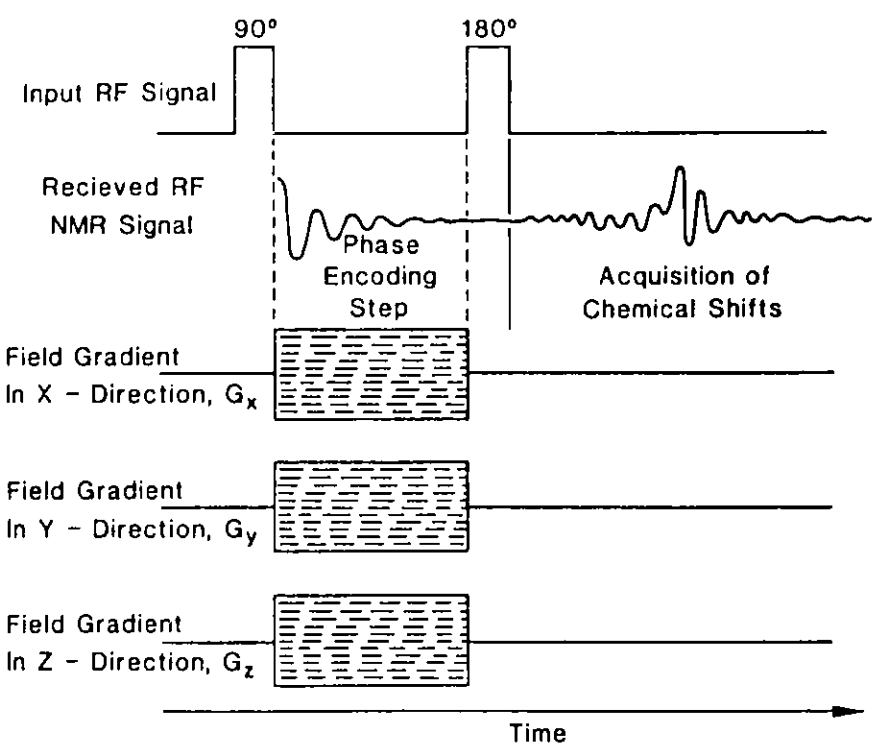

Fig. 8. Chemical-Shift Encoding Based on Fourier Imaging Principles. All spatial encoding occurs by phase encoding during the evolution period. Chemical shifts are frequency encoded during the acquisition period. (After Rothwell et al., Ref. 14.)

1983.[22] Szeverenyi and Macial[19] have successfully developed and tested analogous pulse sequences for ^{13}C chemical-shift imaging of solids.

III. DIRECT NMR IMAGING OF BINDER/PLASTICIZER DISTRIBUTION

Because the polymeric organic B/Ps used in green-state compacts contain a high concentration of protons, they are potential candidates for NMR imaging. We have therefore explored means of direct imaging of these components, with consideration given to the difficulties discussed earlier relative to NMR imaging in solids. We used both a medical imager and an experimental small-bore imager on a number of specimens containing various amounts of B/P.

A. Medical Imager

The medical imager used for the following experiments was a 1.5-T superconducting-magnet NMR imaging system (Siemens Magnetom™). For our first series of tests, a green-state specimen was made by mixing Stark SiC powder with 25 wt.% B/P (PEG, mw = 8000). This is an unusually high loading, but was used for initial tests to ensure adequate proton abundance. The SiC/PEG mixture was cold-pressed at 517 MPa (7500 psi) at room temperature to obtain a right circular cylinder 25 mm in diam and 25 mm high. As shown in Fig. 9, five 5-mm-diam glass beads were incorporated at the midsection of the specimen to simulate defects. Standard (medical imaging) spin-echo and inversion recovery pulse sequences were used to obtain T_1-weighted, T_2-weighted, and proton density-weighted images. The slice thickness was 5 mm and the in-plane resolution was 0.59 mm.

Fig. 9

Schematic Diagram of SiC/25 wt.% PEG Green Ceramic Used in Initial Test of Direct NMR Imaging of B/P.

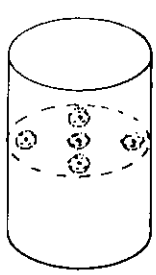

Figures 10 and 11 are transaxial and axial images, respectively, obtained with a T_1-weighted spin-echo sequence (repetition time TR = 0.5 sec, TE = 17 msec, pixel size = 600 μm). The imaging time for Figs. 10 and 11 was 4.3 min (4 excitations x 128 phase-encoding steps x 0.5-sec TR). Not only are the five glass beads well-visualized, but the image inhomogeneity in the surrounding matrix suggests a nonuniform B/P distribution. The T_2-weighted (second echo) images had very low S/N ratios, indicating a relatively short T_2 relaxation time (on the order of one TE) for the B/P. The S/N ratios were also low for the proton density-weighted images, which were made with a longer TE of 28 msec. The in-plane gradients used for phase and frequency encoding were 0.52 gauss/cm. The field homogeneity of the magnet itself in the imaging volume was ~1 ppm.

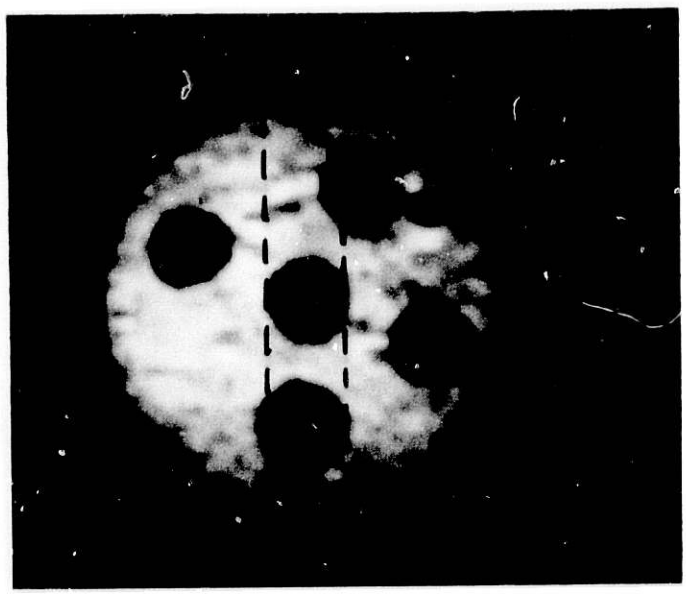

Fig. 10

Tomographic NMR Transaxial Image of Midsection of Specimen Shown Schematically in Fig. 9. The dark circles are the 5-mm-diam glass beads. The image also reveals inhomogeneous B/P distribution in the SiC matrix.

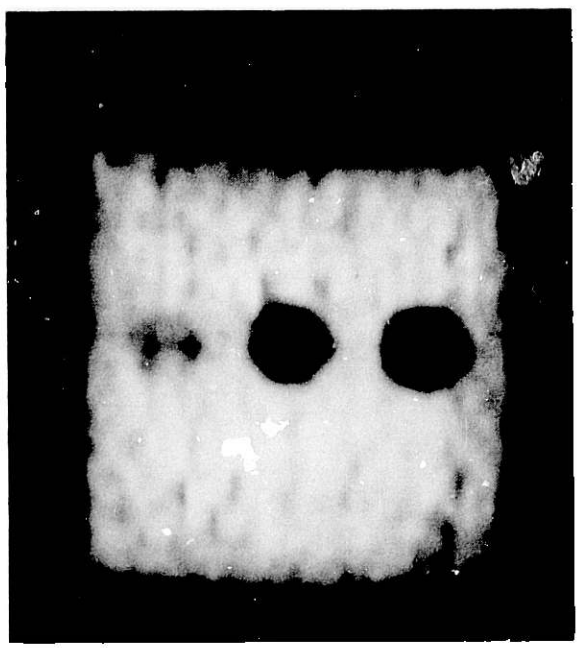

Fig. 11

Tomographic NMR Image of Axial Plane of Specimen Shown in Figs. 9 and 10 (see Fig. 10 for axial plane location). The axial location of the glass beads is clearly detected.

For our second series of experiments with the medical imager, Si_3N_4 powder was mixed with 15 wt.% of a proprietary B/P. The mixture was ground into small (1-3 mm), irregularly shaped pieces, and two test specimens, each 25 mm in diameter and 25 mm high, were made from this pelletized material. Prior to the imaging tests, we conducted a series of linewidth tests in a 7.1-T, 300-MHz Bruker Model 300AM variable-temperature (VT) NMR spectrometer to establish the T_2 values. We suspected that elevated temperature would be necessary to increase T_2 to values close to those necessary for medical instruments, i.e., ~10-15 msec. We first conducted an NMR spectral linewidth experiment (using a simple 90° pulse sequence) to look for differences between B/P alone and the Si_3N_4-B/P mixture. The relation

$$\Delta_{1/2} \simeq \frac{1}{\pi T_2^*} \qquad (6)$$

was used to correlate T_2^*, where $\Delta_{1/2}$ = is the FWHM of the amplitude vs. frequency trace and T_2^* is the estimated (denoted by *) characteristic time constant for loss of phase coherence among spins oriented at an angle to the vector of the main magnetic field, B_o. The results for B/P alone and the Si_3N_4-B/P mixture are shown in Table 2. For the combined Si_3N_4-B/P system, the T_2 values are well below 1 msec even at elevated temperatures, i.e., nearly 2 orders of magnitude smaller than those necessary for reasonable S/N ratios on a commercial medical NMR imager.

Table 2. Effect of Temperature on T_2^* (Spin-Spin) for B/P Alone and Si_3N_4 + 15 wt.% B/P

Temperature (°C)	FWHM (Hz)	T_2^* (ms)
	B/P Alone	
23	1000	0.32
42	1000	0.32
47	800	0.40
49	700	0.45
51	640	0.50
53	580	0.55
55	550	0.58
60	313	1.02
100	11	29.00
	Si_3N_4 + 15 wt.% B/P	
20	3700	0.09
30	3700	0.09
45	2840	0.11
60	1490	0.21
70	1420	0.22
100	1400	0.23

In general, the NMR spectral linewidth in a normal, solid state is likely to be quite broad owing to dipole-dipole interactions between the nuclei of interest.[6-8] Since the size of a coupling is proportional to the magnetogyric ratio of each spin of a coupling pair and inversely proportional to the cube of the separation between the pair, increases in molecular motion (and hence separation) due to elevated temperature will narrow the NMR linewidth. This behavior was confirmed by the spectroscopy tests on the 7.1-T Bruker NMR spectrometer at 100°C. A relatively sharp NMR peak (FWHM of ~11 Hz) was obtained for the B/P, as shown in Fig. 12. The chemical shift (ξ) is calculated as follows:

$$\xi \text{ (in ppm)} = \frac{\text{observed shift (in Hz)} \times 10^6}{B_o \text{ (in Hz)}} , \qquad (7)$$

where B_o = 300 MHz in a 7.1-T field and ξ = 0 ppm for tetramethylsilane (TMS), which is used as a reference.

We also conducted a series of "real" T_2 measurements (i.e., not estimated, as in the spectral linewidth studies) on the B/P itself and on the Si_3N_4-B/P mixture. We used a Hahn spin-echo pulse sequence, which is represented by

$$D_1\text{-}t(90°)\text{-}\tau\text{-}t(180°)\text{-}\tau\text{-FID} \quad , \tag{8}$$

where D_1 is the time required to relax to equilibrium ($\sim 5T_1$ for complete relaxation; a value of 2 sec was used), τ is the variable delay time, and t(90°) and t(180°) are pulse durations. The results as a function of temperature are shown in Table 3, and T_2 values for the binder alone are plotted as a smooth curve in Fig. 13. The increase in T_2 with temperature indicates that the mobility of H protons in the wax-like B/P increases with temperature.

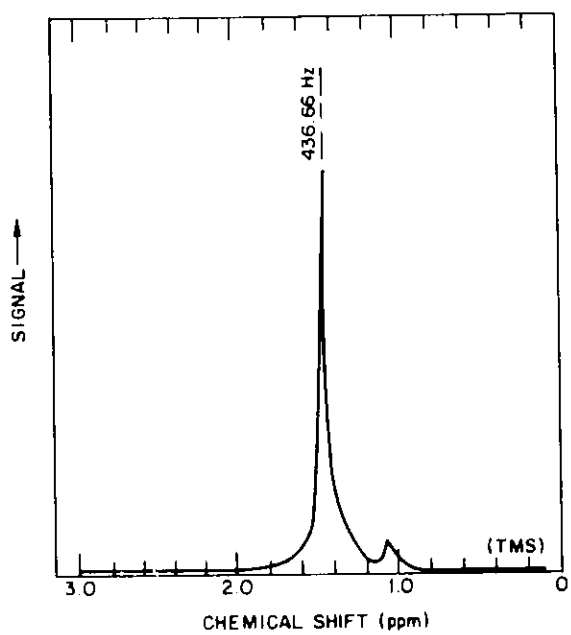

Fig. 12

NMR Spectral Linewidth of Organic Binder at 100°C, as Determined with a VT NMR Spectrometer (No Magic Angle Spinning).

Table 3. Effect of Temperature on T_2 for B/P Alone and Si_3N_4-B/P Mixture[a]

Temperature (°C)	T_2 (msec)	
	B/P	Si_3N_4 + B/P
22	0.26	0.24
40	0.52	0.35
60	12.35	0.69
80	43.00	N/A
100	69.00	N/A

[a] T_2 was measured with a 7.1-T spectrometer and a Hahn pulse sequence.

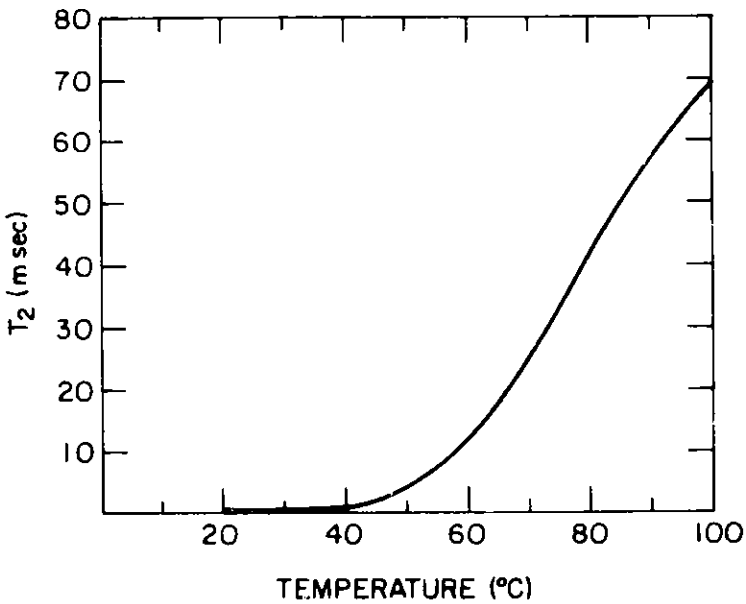

Fig. 13

A Plot of the Data of Table 3 for B/P Alone.

In order to understand the impact of static magnetic field and magnetic gradient on T_2 values, we also measured the T_2 of the B/P at room temperature (22°C) with a 2-T GE Chemical Shift Imager. A Hahn spin-echo pulse sequence was again used. In Fig. 14, the results of this measurement are compared with the T_2 values obtained with the 7.1-T Bruker NMR spectrometer at the same temperature.

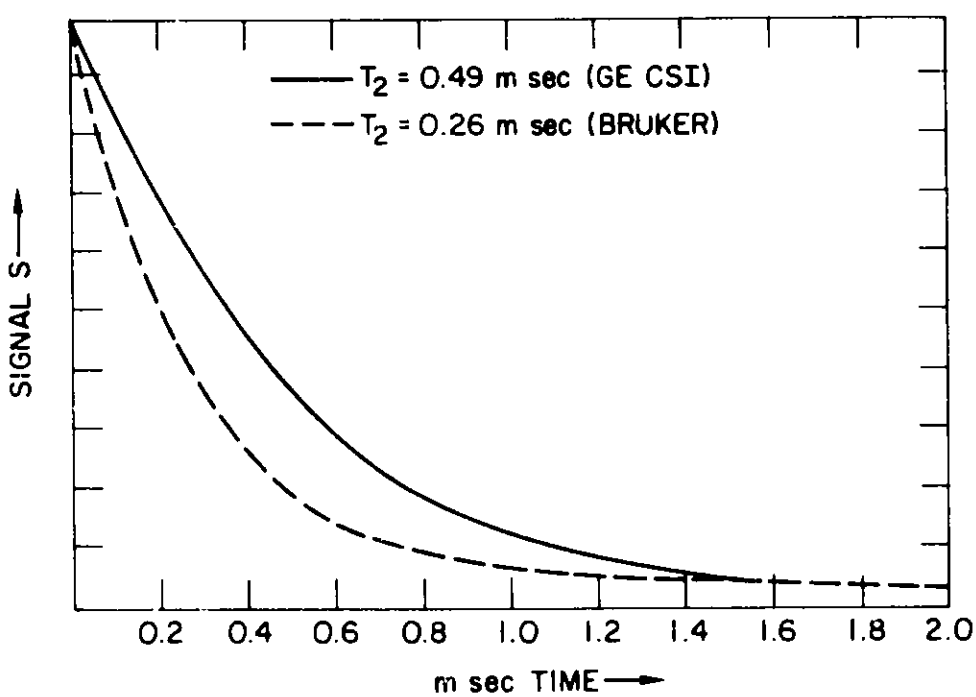

Fig. 14. Comparison of Room-Temperature T_2 Measurements of Organic B/P Obtained with the Bruker NMR Spectrometer (7.1 T) and with the Spectrometer Mode of the GE Chemical Shift Imager (2 T).

Because of the narrower linewidth (better resolution) and higher T_2 value (closer to the level required by the medical imager) obtained for the B/P in elevated-temperature experiments, consideration will be given to direct NMR imaging of B/P and Si_3N_4-B/P mixture at elevated temperature.

We experimentally verified the difficulty of imaging low-T_2 materials by placing the Si_3N_4-B/P specimen in a glass vial and heating it by immersion in hot water. The vial and hot water were placed in a Styrofoam container which fit snugly inside the circular eye coil (Fig. 15). We conducted two imaging studies, one at 50°C and one at 80°C. In the 50°C test, routine medical imaging techniques were used with T_1-weighting,* TR = 0.5 sec, TE = 17 msec, 5-mm slice thickness, and 2 acquisitions in a spin-echo mode. The resulting NMR image (Fig. 16) shows the B/P itself (very bright, 100-200 times background), the ceramic-B/P system (no detectable signal), and a test specimen of the 8000-mw PEG alone. Clearly, at the 15 wt.% B/P loading at 50°C, the protons are not sufficiently mobile to produce a useful image. Figure 17 shows an NMR image of a set of samples

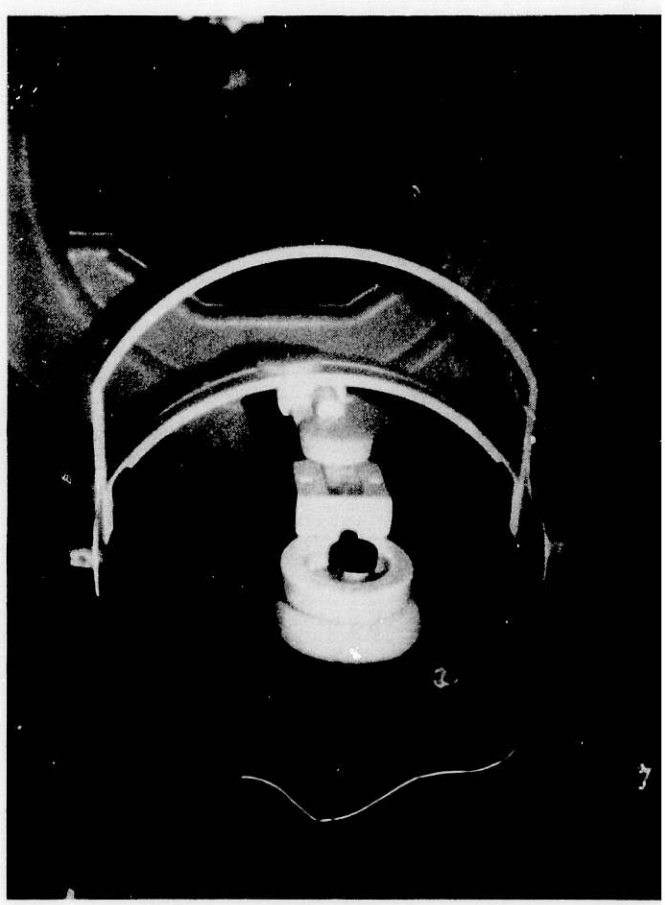

Fig. 15

Glass Vial, Containing Ceramic-B/P System, in Orbit Coil Prior to Placement in Primary Magnet Gantry.

*In medical terminology, T_1-weighting designates a reduced T_1 effect. T_2 values in human tissues are of the order of 50-25 msec, so in the medical imaging context, the combination of short (<1 sec) TR and short (<30 msec) TE produces a T_1-weighted image. In the context of B/Ps with T_2 of the order of 1 msec, such parameters produce an image that is heavily T_2-weighted.

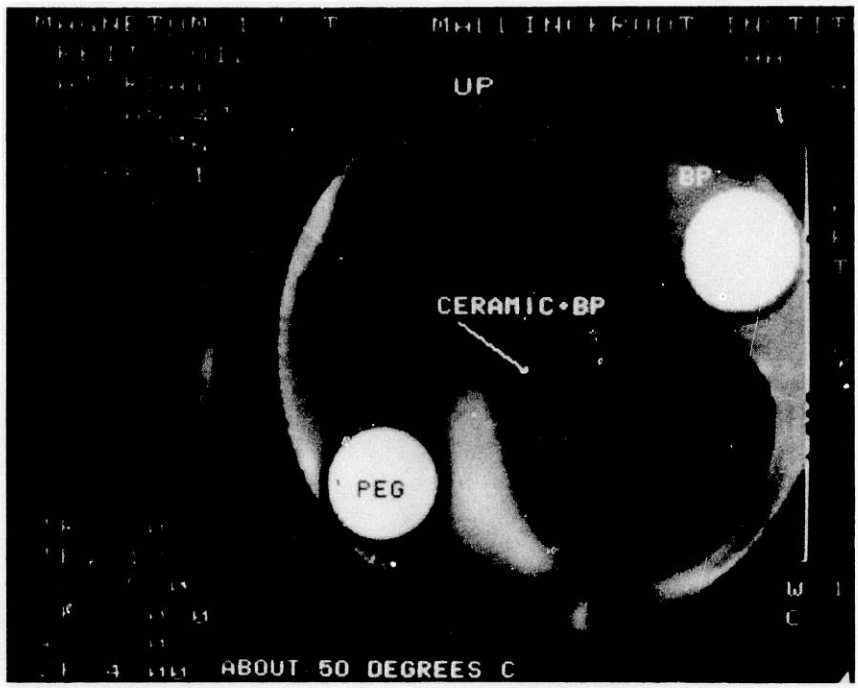

Fig. 16. NMR Image of Proprietary Ceramic-B/P System, B/P Alone, and a Test Specimen of 8000-mw PEG, Obtained with Test Samples at ~50°C.

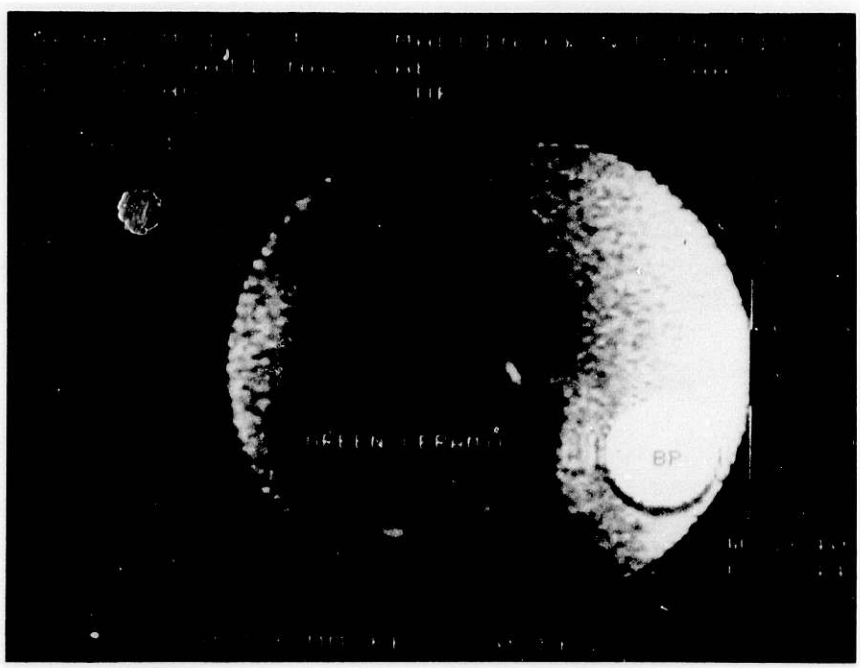

Fig. 17. NMR Image of Proprietary Ceramic-B/P System and B/P Alone, Obtained with Test Samples at 80°C.

similar to the one shown in Fig. 16 but at 80°C. The signal strength is again 100-200 times background for B/P alone; for B/P in the ceramic, it is now ~10 times background, but still not large enough to be useful. The light region around the ceramic-B/P specimen may be water vapor, since the specimen was heated in water.

B. Experimental Small-Bore Imager

It is possible to circumvent the resolution-degrading effects of broad spectral lines and frequency-encoded projections by using special techniques that involve pulsed-field-gradient phase encoding or its equivalent for all spatial dimensions. However, such techniques are difficult if not impossible with a medical imager. Emid and Creyghton[18] used phase encoding to produce one-dimensional images in surfactant systems with intrinsic linewidths of 2 kHz. The single phase-encoded dimension in conventional NMR images is typically free of line-broadening effects, whereas the frequency-encoded dimension displays reduced resolution because the true projections of the object are convolved with the broad spectral lineshapes of the intrinsic NMR signal.

As mentioned in the Introduction, the shortest TEs obtainable with standard imaging equipment are in the range of 12-17 msec. Since the T_2 of polymeric B/Ps tends to be on the order of one msec or less, we confirmed by experiment[12] that it was essentially impossible to obtain images of such B/Ps by conventional means. However, B/Ps with a high plasticizer (e.g., water) content can be imaged; in this case, we are imaging primarily the fluid water in these materials. We have imaged such specimens, and find that after they were allowed to dry, no echo signal could be obtained with TEs of more than 10 msec. Therefore, when the level of plasticizer is high, clinical instruments may be useful for B/P imaging. When the content of molecularly mobile compounds in the B/P is low, however, it becomes necessary to resort to special techniques and apparatus.

To enable the imaging of conventional polymeric B/Ps in green ceramics, we have designed and fabricated a special NMR probe in cooperation with Doty Scientific, Inc. This probe has three important features. First, it has an RF coil that is substantially smaller than the 10-cm-diam coil normally used with the Technicare Corp. system. The new RF coil has an active volume that is cylindrical in shape, with a diameter and length both equal to 3 cm. The coil axis is oriented perpendicular to the direction of the main magnetic field (solenoidal configuration) to enhance the sensitivity of the measurement. With 100 watts of RF power (our usual maximum level), we obtain a 90° pulse length of 6 μsec; this compares with an RF pulse length of approximately 50 μsec for a standard whole-body coil. This represents nearly an order-of-magnitude improvement in RF performance. The detected S/N ratio is expected to behave similarly. The short RF pulse length is necessary for uniform excitation of the broad spectral lines of solid materials.

Second, this probe has its own set of magnetic field gradient coils which are used in place of the standard coils. Because of the smaller coil volume, the same currents will produce much more intense field gradients. Thus, whereas our normal field gradients are ~1 G/cm, our maximum field gradients with the smaller coil are on the order of 10 G/cm or greater. The probe is capable of producing field gradients on the order of 60 G/cm at low

duty cycles. An additional feature of the gradient coil system is that the coils are self-shielded, i.e., the gradient coils are actually wound in pairs so that the outer coil of each pair cancels the external field gradient produced by the inner coil. This reduces the induced eddy currents in the magnet structure and allows the field gradients to be switched much more quickly. The smaller size of these coils also reduces their inductance, which contributes to faster switching speed. This new set of gradient coils reduces our minimum TE from about 15 msec for the 10-cm-diam gradient coil set to below 2 msec (the 2-msec limitation is due not to the new gradient coils, but rather to the minimum time interval allowed in the pulse programming of this instrument).

With the special probe, we have used a spin-echo pulse sequence with phase encoding of both spatial dimensions to avoid the effects of spectral line broadening. In contrast, standard spin-echo sequences[24] may have reduced resolution along the frequency-encoding dimension because the true projections of the object are convolved with the broad spectral lineshapes of the intrinsic NMR signal. In principle, equivalent overall performance should be achievable with standard and double phase-encoding pulse sequences. However, instrumental limitations generally tend to favor double phase encoding for very short TE. The double phase encoding becomes essential when the NMR spectrum becomes complicated, because this sequence uncouples the details of the NMR spectrum from the spatial resolution in the image. A drawback of double phase encoding is that it can require a dramatic increase in imaging time: from minutes for two-dimensional NMR to hours for three-dimensional NMR imaging techniques. We have applied both types of sequences to find the best compromise between the key factors of time and spatial resolution.

Figure 18 shows a transaxial NMR image of a green compact with 15 wt.% B/P (for a test of the imaging technique). A two-dimensional spin-echo RF pulse sequence was used with no slice selection applied and a TE of 4.42 msec. In this sample, we drilled several holes with diameters ranging from 1.1 to 4.8 mm. During these tests, we used 40 signal averages per phase-encoding gradient step with a total imaging time of 29.3 min. The TR was 300 msec. The digital resolution in the image is 128 x by 128 y pixels,

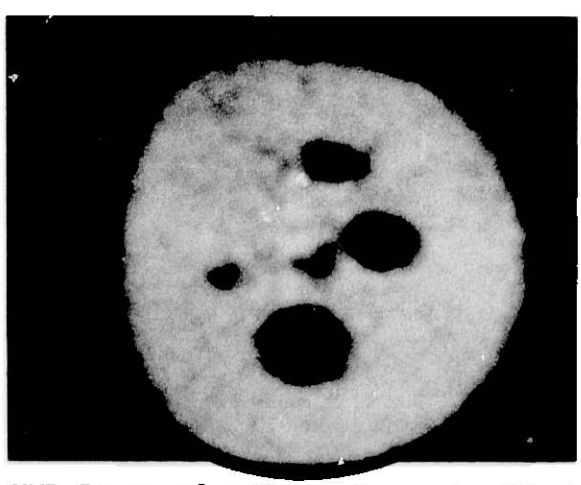

Fig. 18. Transaxial NMR Image of a Green Compact with 15 wt.% B/P, Taken with a Two-Dimensional Spin-Echo RF Pulse Sequence. TE = 4.42 ms; 40 signal averages = total imaging time of 29 min.

corresponding to 640 μm in either direction. The x resolution (along the frequency-encoding direction) will be degraded by the broad spectral linewidth of the B/P material. (The image does not look perfectly symmetric because of a nonlinearity in one field gradient coil, which is now being corrected.)

Figure 19, which is a transaxial NMR image of the sample shown in Fig. 18, was obtained by using a three-dimensional spin-echo sequence having phase-encoding gradients in two dimensions. No slice selection was applied, and TE was 4.42 msec. Two signal averages were taken per phase-encoding gradient step and the total imaging time was 30.4 min. The image resolution is 64 x 64 pixels or 690 μm in both axes.

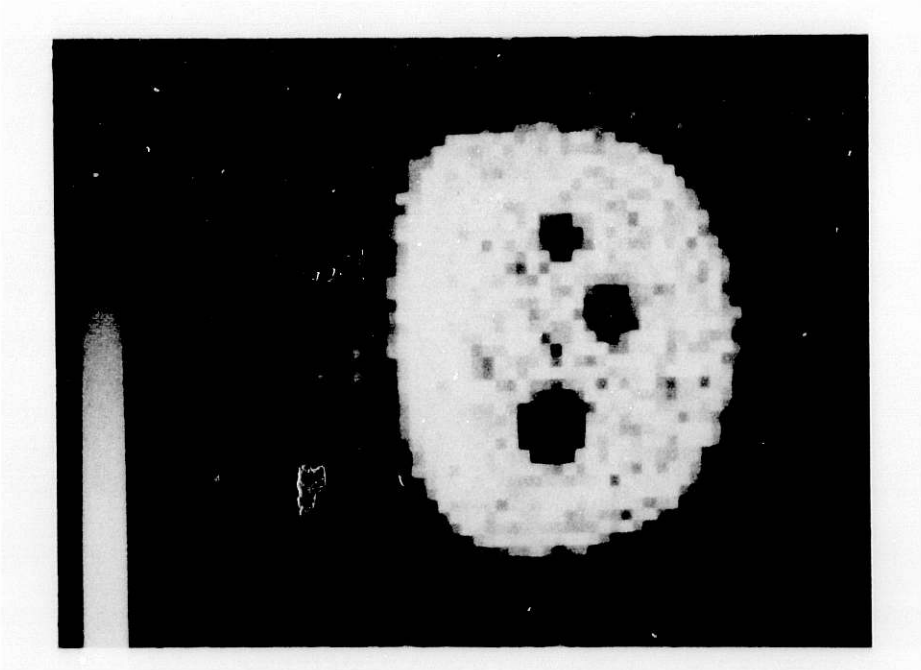

Fig. 19. Transaxial NMR Image of the Same Sample Shown in Fig. 18, Taken with a Three-Dimensional Spin-Echo RF Pulse Sequence. TE = 4.42 msec; 2 signal averages = total imaging time of 30 min.

Both sequences produce images with similar spatial resolution. However, for a given imaging time, the two-dimensional spin-echo sequence produces images with a higher S/N ratio than a three-dimensional spin-echo sequence, increasing the contrast between regions with possible differences in the concentration of B/P. Thus, it is easier to see small features in the former case (Fig. 18) than in the latter case (Fig. 19). Although the blocky appearance of the image obtained with the three-dimensional acquisition (Fig. 19) might suggest that its resolution is lower, such is not the case. The three-dimensional image has a small number of pixels with a point spread function only one pixel wide, whereas the two-dimensional image has a larger number of pixels with a point spread function covering several pixels.

It is possible to achieve a higher resolution and S/N ratio in three-dimensional spin-echo sequences, but the imaging time increases dramatically

owing to the need for extra signal averaging. Figure 20 shows a transaxial B/P image obtained with one such sequence. The specimen is a green alumina compact with a length to diameter (L/D) ratio of 0.17 and a mean particle size of 4.5 mm. Note especially that the concentration of B/P is only 2.5 wt.%. No slice selection was employed and TE was 3.2 msec. Sixteen signal averages were taken for each phase-encoding gradient step, for a total imaging time of 17 h. The resolution is 127 x 128 pixels or 330 μm in both in plane dimensions.

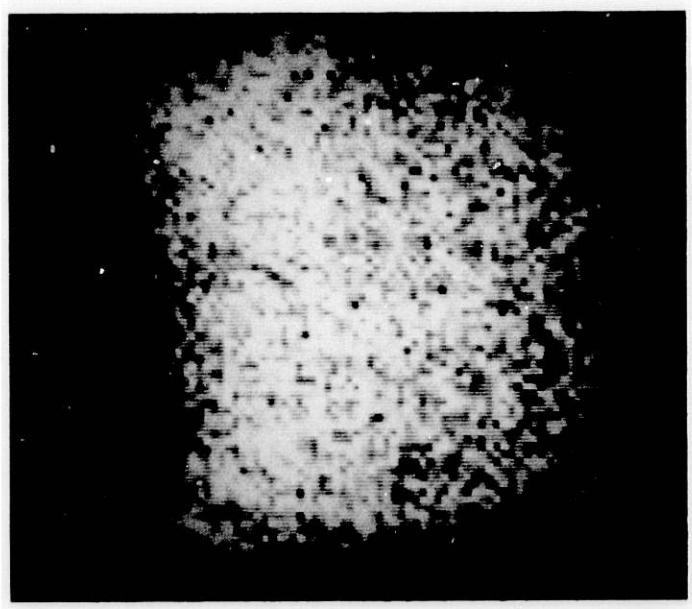

Fig. 20. Double Phase-Encoded Image of 25-mm-diam Al_2O_3 Sample with 2.5 wt.% B/P, Taken With Special Probe and TE = 3.2 msec. Image resolution is 128 x by 128 y pixels (310 and 340 μm, respectively). Total data acquisition time was about 17 hours.

IV. POROSITY MEASUREMENTS

After removal of the organic B/P from green ceramics, open porosity remains. The distribution of this open porosity provides insight into how the specimen will densify. Although mercury porosimetry has long been used to obtain porosity measurements, it has two limitations: (1) it is limited to small (<1 cm^3) specimens of regular shape and (2) it does not yield tomographic (i.e., spatial) information. NMR imaging, on the other hand, has the potential to provide not only tomographic (i.e., three-dimensional) information, but also information on specimens of any size and shape.

The use of a filler fluid to image the internal empty volume of dewaxed ceramics was discussed in the Introduction. The fluid is introduced into the test samples, contained in a 38-mm-OD x 51-mm-long glass tube, by vacuum impregnation. In using this technique, we assume adequate penetration of the filler fluid into all the internal volumes of interest, including pore spaces and internal voids. Penetration is assisted by using a fluid of low viscosity and low interfacial tension with the microscopic surfaces of the sample.

The filler fluid approach provides a means to visualize internal volumes that are larger than the spatial resolution of the measurement, which is about 300 μm within the image plane for the measurements presented here. Volumes with the in-plane dimensions smaller than the in-plane resolution (specifically, the microscopic volumes that constitute the pore structure) are not resolved. We take the fractional porosity to be equal to the fractional image inten- sity (i.e., image intensity normalized to the intensity of pure filler fluid).

A. Samples and Filler Fluids

The use of filler-fluid NMR for porosity imaging was studied with ceramic samples prepared at the ALCOA Laboratories, Argonne National Laboratory, and the National Bureau of Standards. Sample 1 was a green-state MgO compact, made by cold pressing 309 g of MgO powder and 20% PEG (mw = 3200) into a 31-mm-diam x 27-mm-high cylinder at 344 MPa (5000 psi). Six holes, ranging from 330 μm to 1390 μm in diameter, were drilled parallel to the cylinder axis to provide recognizable void features, as shown in Fig. 21. Sample 2 was a 25-mm-diam green-state SiC compact, similarly prepared and drilled. Sample 3 consisted of three partially sintered Al_2O_3 disks, 25 mm in diameter, with densities of 1.648, 1.703, and 1.720 g/cm^3, respectively. Sample 4 consisted of two sets of Al_2O_3 disks specially prepared by ALCOA. The powders used in the two sets had mean particle sizes of 4.5 and ~0.4 μm, respectively. Each set consisted of three sample groups with a green-state diameter of nominally 25 mm and L/D ratios of 0.17, 0.58, and 1.13, respectively. (Different powder sizes and different L/D ratios were used to see whether the NMR porosity measurements were sensitive to these parameters.) Each group consisted, in turn, of three different types of specimens with nominal densities as follows: (a) green, 56.4% theoretical density; (b) bisque-fired, 54.9% theoretical density; and (c) partially sintered (prepared by heating bisque-fired compacts), 86.5% theoretical density. All samples were prepared in a single-ended press at a pressure of 689 MPa (10,000 psi). The bisque-fired and partially sintered specimens are dewaxed; the green-state specimens are not.

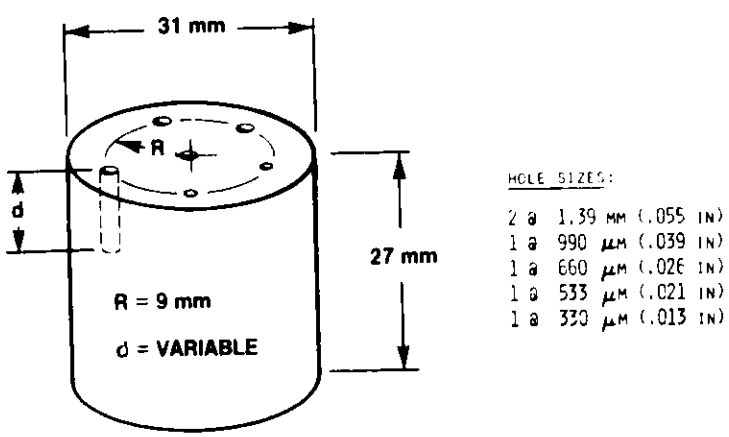

Fig. 21

Schematic Diagram of MgO Test Phantom Used for Initial NMR Porosity Imaging Studies.

Preliminary work was done on various filler fluids, including hexafluorobenzene. Because of the high cost of hexafluorobenzene and lack of suitable paramagnetic dopants, we chose to work with benzene, which is con-

siderably less expensive, easier to dope, and sufficiently compatible with the binder. The proton molarity of benzene was 67.3 M, which provided a reasonably high proton concentration (that of water is 111 M). Paramagnetic doping was with chromium acetylacetonate, $Cr(CH_3COCH_2COCH_3)_3$, at 10.3 ± 0.6 or 20.6 ± 1.2 mM to give proton T_1s of 237 ± 12 or 122 ± 11 msec, respectively. These relaxation times were determined on a 3.52-T (150-MHz) Nicolet spectrometer, and are expected to be close to the relaxation times at the field strength of the imager.

B. NMR Imaging

The NMR imaging tests with filler fluids were performed on a Technicare Corp. developmental NMR imaging instrument with a magnetic field strength of 1.45 T (61.538-MHz proton frequency). A standard spin-echo pulse sequence[13] with a short TE of 15 msec was used to minimize signal intensity loss due to diffusion of benzene molecules through the interfacial field gradients that exist at the magnetic susceptibility discontinuities of the sample.[16] The pulse TR was ~100 to 200 msec. The digital resolution in the images was 512 x pixels by 256 y pixels, corresponding to pixel sizes of 380 μm in the x-direction by 350 μm in the y-direction. The slice thickness was ~2 mm. The test samples typically span the order of 100 pixels in these images. The slight out-of-roundness in some images is due to magnetic field inhomogeneity (spatial nonuniformity) and magnetic field gradient nonlinearity, which are currently being improved. We determined that under our imaging conditions, i.e., room temperature, magnetic field strength of 1.5 and 2.0 T, and RF pulse sequences as described above, the PEG binder gave no NMR signal. Typical imaging times for the benzene were ~100 to 200 msec, corresponding to 2 or 4 signal averages per phase-encoding gradient step. Occasional images were taken with up to 64 signal averages for improved S/N ratio; these required on the order of one hour. We measured signal intensities over regions of interest and calculated the averages directly from the stored NMR data and not from video brightness or film densities.

Figure 22 is a transaxial NMR image of sample 1, the MgO sample shown schematically in Fig. 21. The plane of the image lies about 1 mm from the face of the sample. The image intensity is an average over the ~2-mm slice thickness. The smallest hole, 330 μm in diameter (on the order of the pixel size), is discernible. The mean porosity of the green compact, as determined from the NMR signal intensity, is 15.5 ± 6.2%. The dark, round patch is suggestive of a region of lower porosity (7.4 ± 1.7%).

Images of sample 2, the SiC sample, are shown in Fig. 23. This sample was inadvertently damaged by freezing of the filler fluid prior to the NMR analysis. The body of the sample was highly fractured, and exhibited a mean NMR-derived porosity of 76 ± 11%. Figure 24 shows the positions of the successive image planes seen in Fig. 23. Image plane a was acquired with 32 signal averages, as opposed to 2 for planes b through e. Some bubbles formed in the drilled holes as a result of the freeze/thaw treatment; these appear as dark regions within the holes of Fig. 23.

An image of sample 3, the set of three partially densified Al_2O_3 disks, is shown in paraxial view in Fig. 25. The image plane approximately coincides with the axes of the disks. NMR signal strength intensities for each disk were measured near the disk axes and near the peripheries, at the

Fig. 22. Transaxial Spin-Echo NMR Image of an MgO/20% Polyethylene Glycol Green Ceramic Compact with the Hole Pattern Shown in Fig. 21. Benzene was used as the filler fluid. The bright rim is pure benzene. The bulk of the ceramic body exhibits an NMR-derived porosity of 15.5 ± 6.2%, and the dark, round patch has a porosity of 7.4 ± 1.7%. The background (noise) value is 2.1 ± 1.1%.

approximate positions shown by the marked regions of the mid-disk. Figure 26 shows the relationship between the NMR-derived fractional porosities and the densities of the Al_2O_3 specimens. The vertical bars on the experimental points represent standard deviations within each region of interest, and the solid lines are linear least-squares fits. The higher porosity and increased porosity variance at the periphery are roughly in accord with what is known about density distributions after compaction.[25]

An experiment was conducted on one Al_2O_3 specimen from sample 4. Specimen F3-L (set number 1, particle size ~0.4 μm, L/D = 1.13), partially sintered to 86.5% of theoretical density, was vacuum impregnated with the paramagnetically doped benzene. A sagittal NMR image of this sample is shown in Fig. 27. The gray-scale values of the individual pixels of the sagittal NMR image correspond to the filler fluid concentration, and hence to the local porosity. The bright region outside the specimen represents the gray-scale value of the pure benzene. By means of this filler-fluid technique, all the L/D = 1.13 specimens from sample 4 were imaged, and the average bulk porosity was determined by normalizing the NMR signal strength to that of pure benzene (which represents 100% porosity). The results are shown in Table 4.

C. Image Processing

To assist in the visualization of NMR image details, histogram representations of the image data were constructed. Analysis by histograms can be used to improve the statistics of, and remove systematic errors from, calculations of fractional porosity by identifying pixels that do not accurately reflect true signal intensities. Histograms can also be used to construct the distribution functions for either B/P concentration or porosity. The image data files produced by the Technicare instrument contain a 256x256-pixel matrix, which is too computationally intensive for the

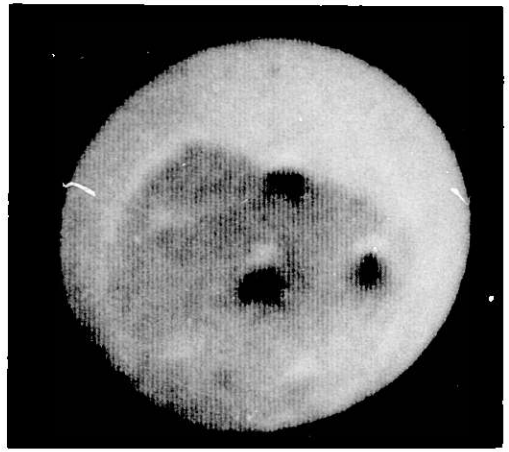

(a)

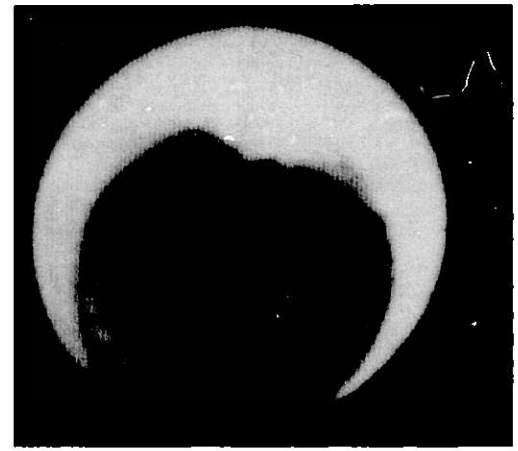

(b)

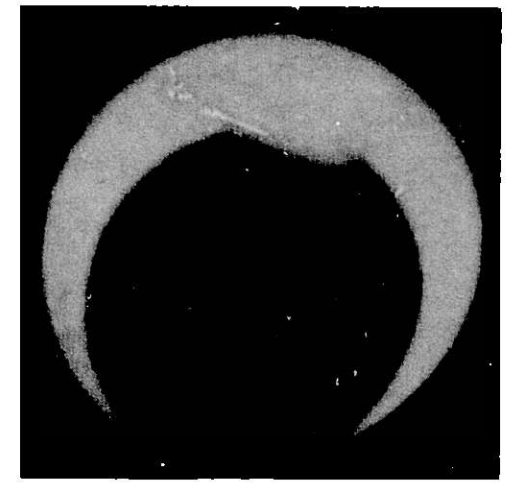

(c)

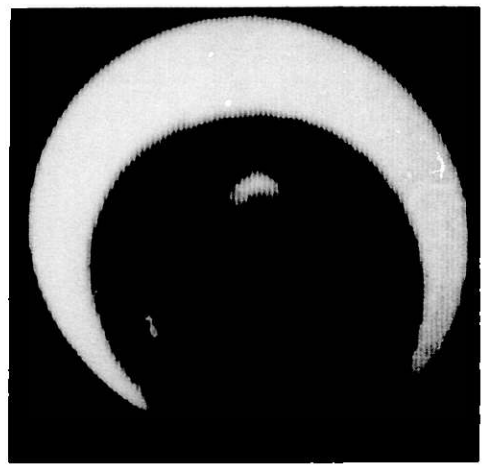

(d)

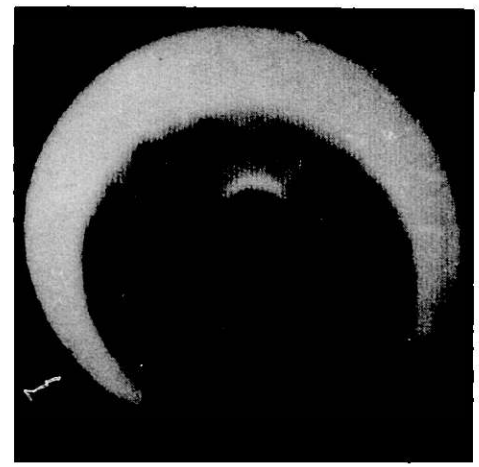

(e)

Fig. 23

A Sequence of Five Image Planes of a Highly Fractured SiC/Polyethylene Glycol Sample, Positioned as Shown Schematically in Fig. 24. The sample is drilled as shown in Fig. 21. Image (a) is made up of 32 signal averages, the others of 2 signal averages each. The mean NMR posority is 76 ± 11%. The dark areas at the holes are air bubbles trapped as a result of the fracturing process.

Fig. 24

Schematic Diagram of the SiC/ Polyethylene Glycol Sample Shown in Fig. 23.

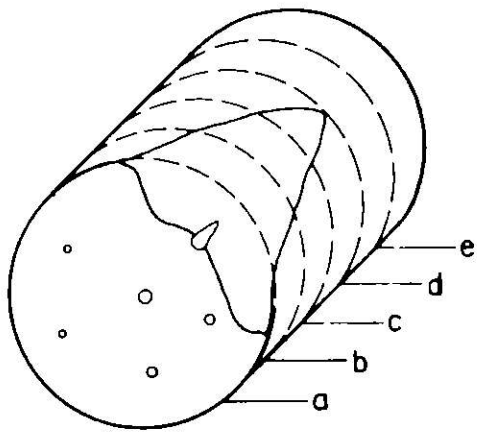

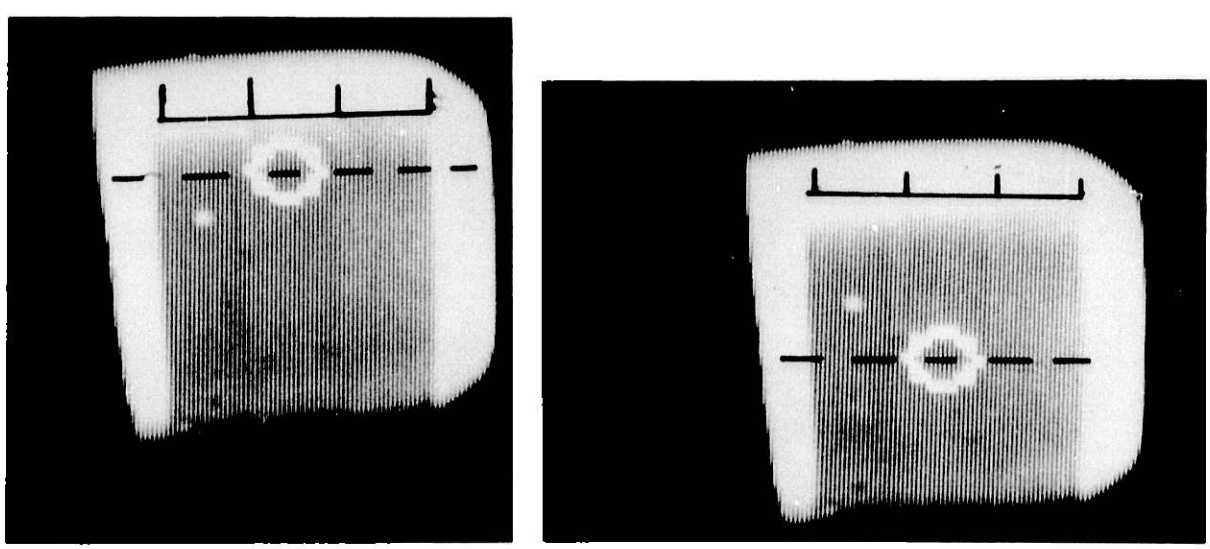

Fig. 25. Paraxial View of Three Partially Sintered Al_2O_3 Disks (Delineated by Brackets) of Measured Density (Right to Left) 1.648, 1.703, and 1.720 g/cm^3. The image plane approximately coincides with the axes of the disks. Dashed lines denote the radial positions where signal intensities were measured.

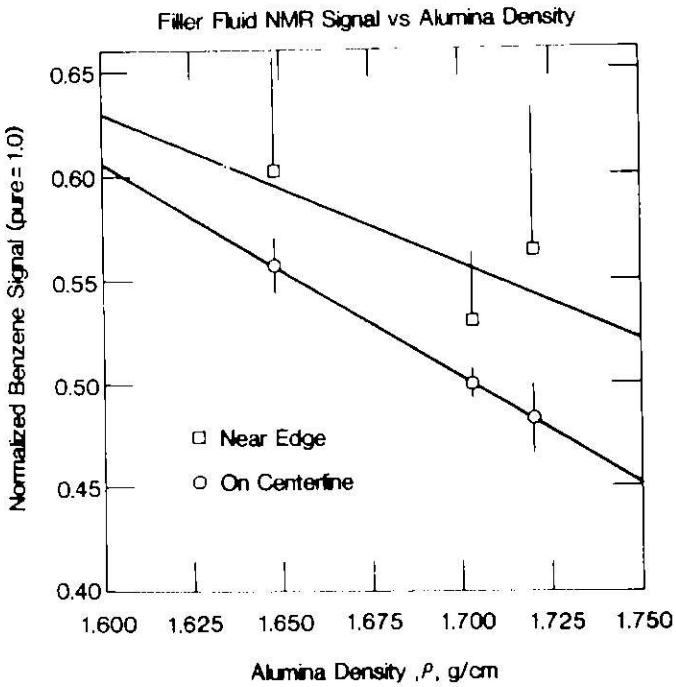

Fig. 26. NMR Signal Intensity vs Measured Density for Three Partially Sintered Al_2O_3 Disks. □, peripheral region; o, on-axis region. Solid lines are least-squares fits; error bars are standard deviations about the mean pixel intensity within each region of interest. (Half-error bars are used where necessary to avoid overlap.)

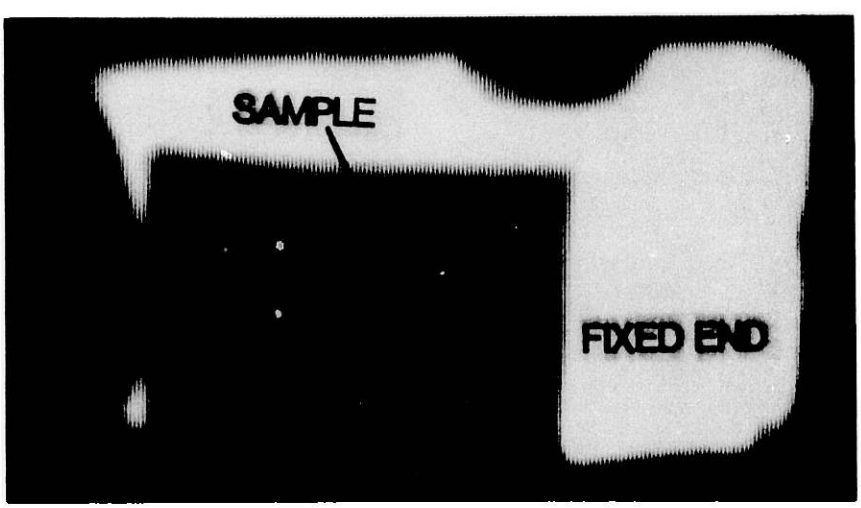

Fig. 27. Sagittal NMR Image of Partially Densified Al_2O_3 (ρ = 3.47, 87% TD, slice thickness = 2 mm).

Table 4. Average NMR-Derived Porosity in Alumina Compacts (Sample 4) with L/D Ratio of 1.13

Sample Reference	Degree of Sintering	Particle Size (μm)	Average Porosity[a] (percent)	Noise (percent)
G1-L	green	4.5	1.1	0.7
G2-L		4.5	1.4	0.7
G3-L		0.4	10.8	0.8
G4-L		0.4	10.6	0.8
B1-L	bisque-fired	4.5	3.0	0.8
B2-L		4.5	3.2	0.9
B3-L		0.4	27.4	1.2
B4-L		0.4	27.8	0.8
F1-L	partially sintered	4.5	2.5	0.8
F2-L		4.5	2.9	1.0
F3-L		0.4	2.2	1.0
F4-L		0.4	2.6	1.0

[a]The porosity was determined on a relative basis with the signal of pure benzene taken as 100%.

present computer. For our image processing tasks, image data files were reduced to a 128x128-pixel matrix by sampling alternate rows and columns.

Figure 28 shows a signal intensity histogram of the NMR porosity data set for test specimen B3-L (see Table 4). The x-axis represents the signal intensity as a percentage of the signal strength from the pixel with the highest intensity in the matrix. Background noise pixels have not been included in the porosity distribution seen in the histogram. Two different populations of pixels, one corresponding to the average of the sample (with a maximum at 26%) and the other to the pure filler fluid (centered at 56%), can be observed. Also seen are "broadwings" in the filler fluid pixel distribution. The histogram distribution arises from several factors. First, instrument artifacts from RF and magnetic field nonuniformities can produce variations of a few percent of the actual signal intensity. Second, dif- ferences in bulk magnetic susceptibility between the fluid and adjacent structures can cause displacement of the apparent position of a feature in the image from the true position along the x-axis (frequency-encoding axis), resulting in constructive and destructive intensity anomalies at the borders of a region (one manifestation of the "chemical shift" artifact). Third, microscopic susceptibility discontinuities within a single voxel can attenuate signals arising from spins diffusing through the magnetic field gradients generated by those discontinuities.[25] Finally, pixels that lie on the boundary between two regions must, of necessity, have mixed values. All of these effects tend to be proportional to the absolute signal strength, and therefore, the artifact distribution width will be highest for the benzene. The effect is most noticeable for populations with smaller numbers of pixels; again, the filler fluid is most severely affected. The distribution of intensity for the fractional porosities within the ceramic part is much more accurately represented.

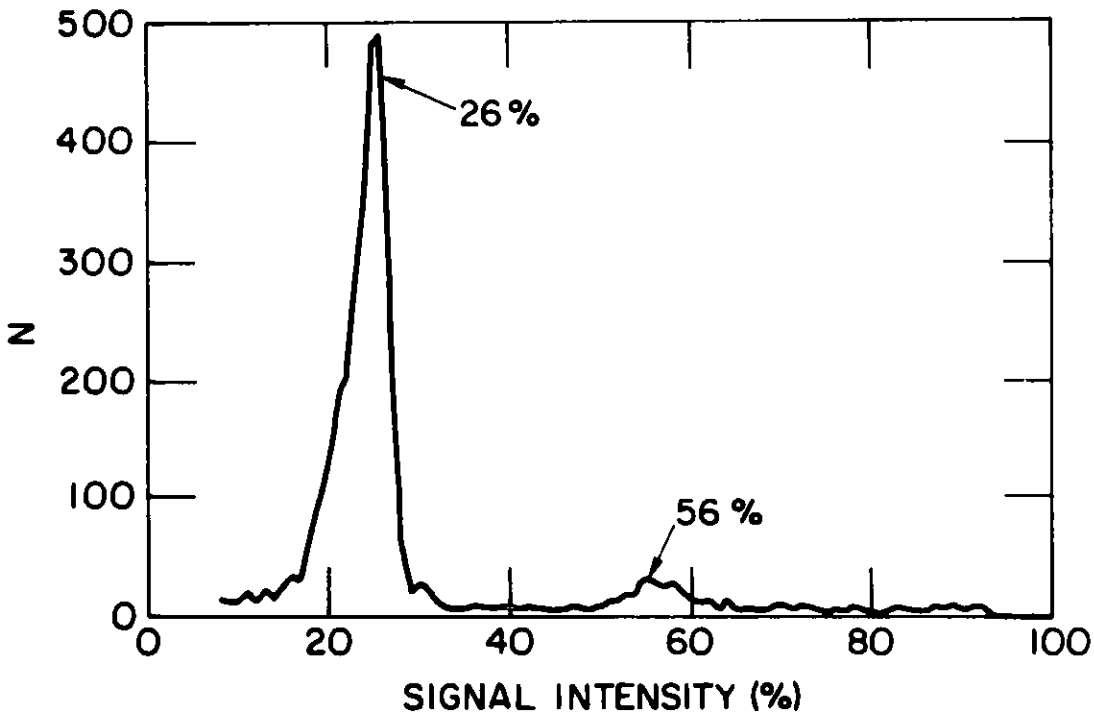

Fig. 28. Histogram Representation of NMR Signal Intensity Data for Bisque-fired Specimen B3-L. The horizontal axis is porosity in percentage with respect to the maximum intensity value in the raw data. The vertical axis represents the number of pixels with the x-axis intensity.

To reduce some of the "edge" effects described above and to obtain a more accurate description of NMR-derived porosity distribution in the sample, a circular region of interest with a diameter that encompasses 93% of the sample diameter was defined. The data were normalized to the mean value of the pure filler fluid obtained from the histogram in Fig. 28. The "wings" of the filler fluid histogram were not included in the mean, since those pixels with extreme values most likely correspond to artifacts caused as noted above. Figure 29 shows the histogram of the same data set as in Fig. 28 but with only those pixels included that are within the region of interest. This technique eliminates many edge effects, since the specimen boundaries and those of the pure filler fluid regions are not included. The x-axis now represents the NMR porosity of the sample and is much more uniform. For comparison purposes, Fig. 30 shows a similar plot for a data set corresponding to a second bisque ceramic specimen (B4-L) with a region of low signal intensity. A long low-intensity "wing" on the histogram distribution function and a wider distribution indicate a less uniform sample.

It should be noted that according to the histogram of Fig. 29, the porosity of specimen B3-L is near 45%, whereas the bulk (average) porosity shown in Table 4 is only 27.4%. The difference reflects the fact that the

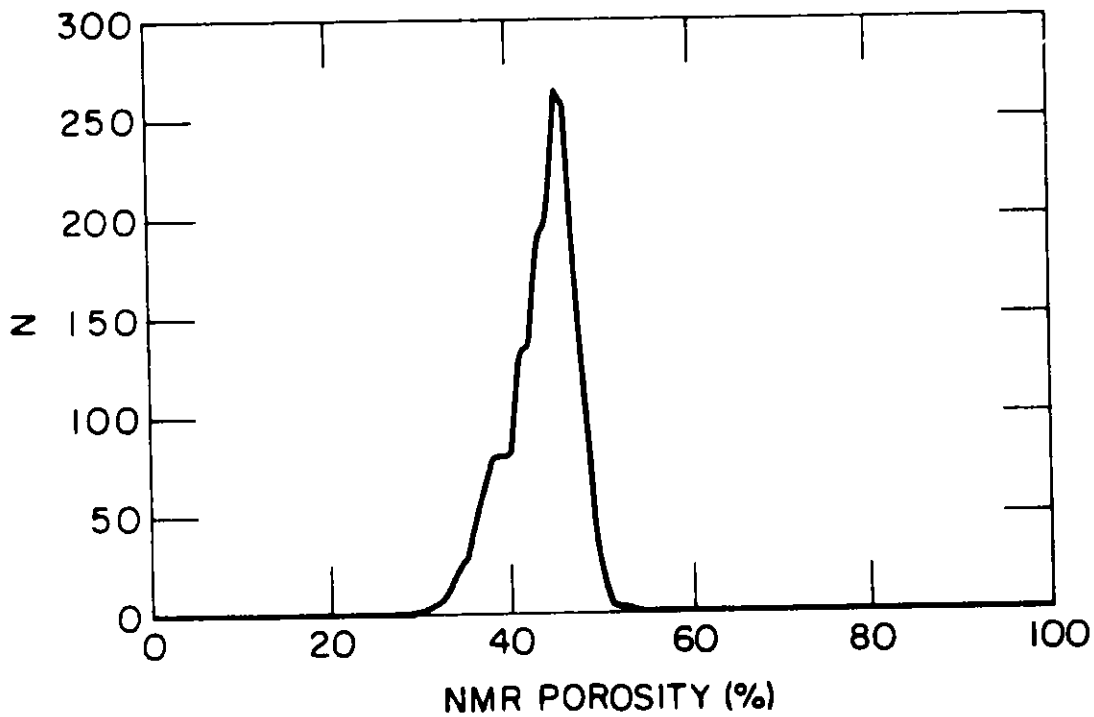

Fig. 29. Histogram of the Same Data Set as Fig. 28 (Specimen B3-L), but Displaying Only the Pixels within a Region of Interest of the Specimen. Most of the edge effects have been removed from the histogram, allowing an accurate porosity distribution function to be constructed. The x-axis of the histogram is normalized to the mean intensity of the filler fluid distribution, and therefore represents the NMR-derived porosity distribution function.

limited region analyzed in Fig. 29 has a high porosity, whereas the 27.4% figure is an average over the entire specimen. The same argument holds for the data of Fig. 30. For sample BL-4, the histogram suggests a porosity of 40%, whereas the bulk porosity is 27.8%. Again, the histogram represents a limited region which clearly has a higher porosity.

Overall, this mode of data representation gives valuable information related to the NMR porosity and hence the uniformity of the sample; a narrow distribution would be indicative of a highly uniform sample.

D. Comparison with Results of Destructive Analysis

Recently, two specimens identical to the one shown in Fig. 27 were destructively analyzed by ALCOA with an optical microscope and image analysis software. The results of these analyses are shown in Fig. 31. To be noted is the qualitative agreement between the destructive measurement and the NMR porosity measurement. The darkness of the central region of the NMR porosity image (Fig. 27) is consistent with the very low porosity measured in that region by destructive analysis. Additional work will need to be done to better understand this correlation.

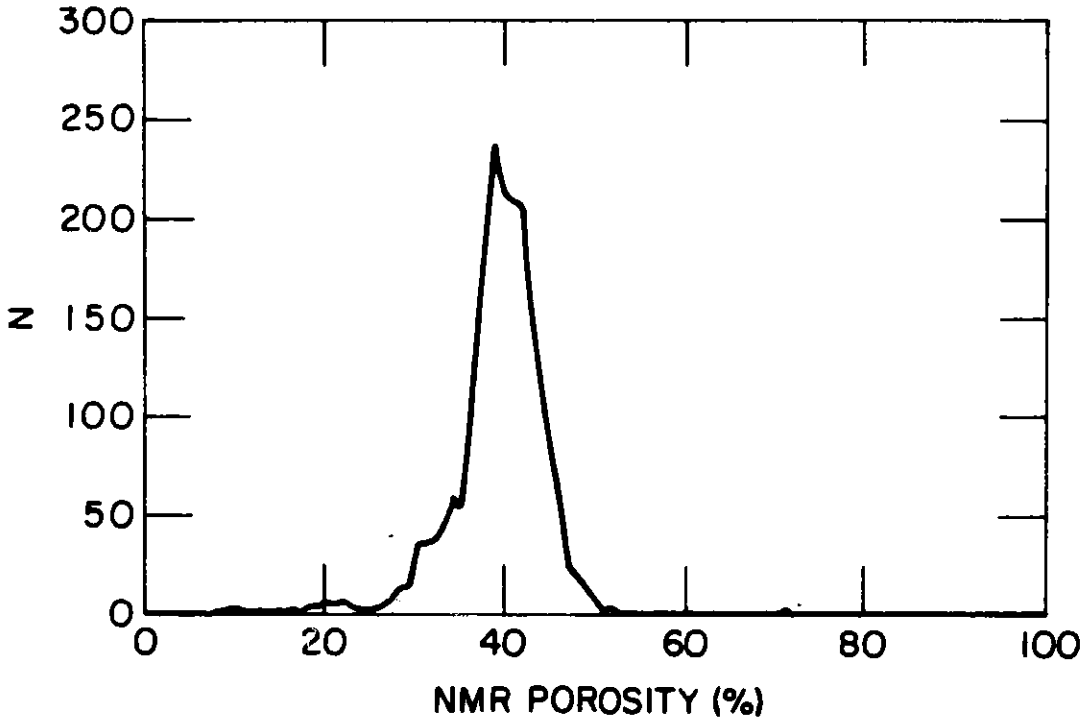

Fig. 30. Histogram of the Data Set Corresponding to a Second Specimen, B4-L. As in Fig. 29, only pixels within the region of interest are plotted.

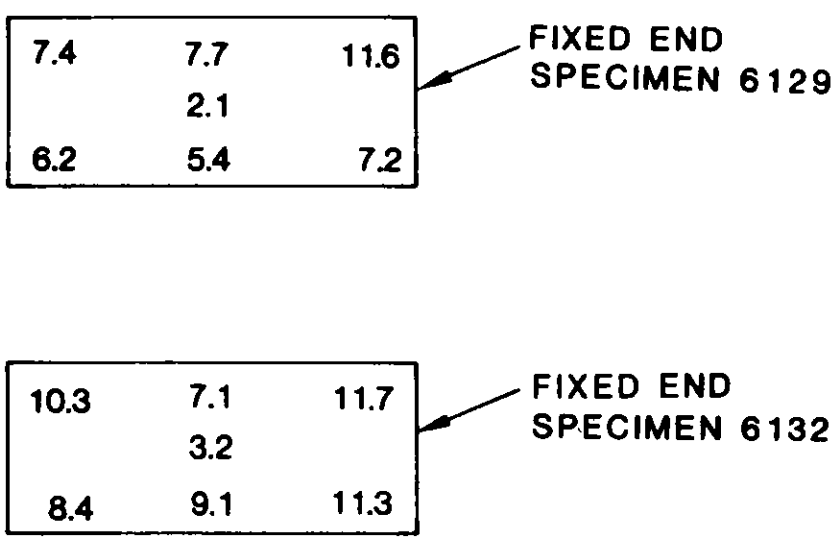

Fig. 31. Porosity Measurements (%) Obtained by Destructive Analysis on Axial Surface of Partially Densified Al_2O_3 Right Circular Cylinder Test Specimens. The specimens are duplicates of the one imaged in Fig. 27.

V. CONCLUSIONS

Direct tomographic imaging of organic B/Ps in ceramic materials can be accomplished by NMR. However, special RF and gradient coil configurations, which obviate the necessity to heat the specimens, need to be used. We have shown that it is possible to image with as little as 2.5 wt.% B/P at 2-T field strength but presently with a sacrifice of tomographic image quality.

Open (surface-connected) porosity can also be tomographically imaged with NMR techniques if appropriate filler fluids are used. We have experimentally demonstrated that qualitative correlations between NMR-measured porosity and porosity measured by destructive analysis can be achieved.

REFERENCES

1. U.S. Congress, Office of Technology Assessment, New Structural Materials Technologies: Opportunities for the Use of Advanced Ceramics and Composites - A Technical Memorandum, OTA-TM-E-32, U.S. Government Printing Office, Washington, D.C., September 1986.

2. H. C. Yeh, J. M. Wimmer, M. E. Huang, M. E. Rorabaugh, J. Schienle, and K. H. Styhr, Improved Silicon Nitride for Advanced Heat Engines, Ann. Tech. Report submitted to NASA by AiResearch Casting Co., A Div. of the Garrett Corp., NASA-CR-175006, October 1985.

3. E. D. Becker, High Resolution NMR, Academic Press, New York, 1980.

4. C. P. Slichter, Principles of Magnetic Resonance, 2nd Ed., Springer-Verlag, New York, 1978.

5. P. C. Lauterbur, Nature 242, 190 (1973).

6. W. A. Ellingson, J. L. Ackerman, J. D. Weyand, R. A. DiMilia, and L. Garrido, Ceram. Eng. Sci. Proc. 8(7-8), 503-512 (1987).

7. J. L. Ackerman, W. A. Ellingson, J. A. Koutcher, and B. R. Rosen, "Development of Nuclear Magnetic Resonance Imaging Techniques for Characterizing Green-State Ceramic Materials," in Proc. 2nd Intl. Symp. on the Nondestructive Characterization of Materials, Montreal, Canada, July 21-23, 1986, pp. 129-137.

8. L. B. Welch, S. T. Gronczy, M. T. Mitsche, L. J. Bauer, J. Dworkin, and A. Giambalvo, "Proton NMR Imaging of Green-State Ceramics," in Proc. Quantitative NDE Conference, La Jolla, CA, D. O. Thompson and D. E. Chimenti, eds., Plenum Press, New York, 1987, pp. 441-456.

9. M. Mehring, High Resolution NMR Spectroscopy in Solids, Springer-Verlag, Berlin, 1976.

10. D. E. Axelson, Solid State Nuclear Magnetic Resonance of Fossil Fuels, Multiscience Limited, Montreal, Canada, 1985.

11. G. R. Finley, J. S. Hartman, M. F. Richardson, and B. L. Williams, J. Chem. Soc. D 159, 67 (1985).

12. W. A. Ellingson, J. L. Ackerman, S. Gronemeyer, and L. Garrido, "Nuclear Magnetic Resonance Imaging for Detecting Binder/Plasticizers in Green-State Structural Ceramics," in Proc. 16th Symp. on Nondestructive Evaluation, San Antonio, TX, April 21-23, 1987, pp. 231-240.

13. S. R. Thomas, L. C. Clark, Jr., J. L. Ackerman, R. G. Pratt, R. E. Hoffman, L. J. Busse, R. A. Kinsey, and R. C. Samaratunga, J. Comput. Assist. Tomogr. 10, 1 (1986).

14. W. P. Rothwell, P. N. Tutjian, and H. J. Vinegar, "NMR Imaging: Nonmedical Applications," in New Directions in Chemical Analysis, B. L. Shapiro, ed., Proceedings of the Third Symposium of the Industry-University Cooperative Chemistry Program of the Chemistry Department of Texas A&M University, March 31-April 3, 1985, Texas A&M Press, College Station, TX, 1985, pp. 366-395.

15. B. H. Suits and D. White, Solid State Commun. 50, 291 (1984).

16. P. Mansfield and P. K. Grannell, J. Phys. C. 6, L422 (1973) and Phys. Rev. 12, 3618 (1975).

17. A. N. Garroway, J. Baum, M. G. Munowitz, and A. Pines, J. Magn. Reson. 60, 337-340 (1984).

18. S. Emid and J. H. N. Creyghton, Physica B&C 128b, 81 (1985).

19. N. M. Szeverenyi and G. E. Macial, J. Magn. Reson. 60, 460 (1984).

20. A. Kumar, I. Welti, and R. R. Ernst, J. Magn. Reson. 18, 69 (1975).

21. W. A. Edelstein, J. M. S. Hutchinson, G. Johnson, and T. Redpath, Phys. Med. Biol. 25, 751 (1980).

22. I. L. Pykett and B. R. Rosen, Radiology 149, 197 (1983).

23. A. A. Maudsley, S. K. Hilal, W. H. Perman, and H. E. Simon, J. Magn. Reson. 51, 147 (1983).

24. P. A. Bottomley, Rev. Sci. Instrum. 53, 1319 (1982).

25. W. D. Kingery, ed., Ceramic Fabrication Processes, The MIT Press, Cambridge, MA, 1963.

Distribution for ANL-87-53

Internal:

R.E. Botto
F.A. Cafasso
S.L. Dieckman
H. Drucker
W.A. Ellingson (15)
D.C. Fee
G. Forster
F.Y. Fradin
S. Gopalsami
E.L. Hartig
T.I. Hentea
E.L. Huang
L.R. Johnson
D.J. Lam
R.L. Larsen
L.A. Neimark
R. Massow
J.A. Morman
M.V. Nevitt
R.B. Poeppel
A.C. Raptis
R.A. Roberts
J.P. Singh
E.M. Stefanski
L. Stock
J. Tang
J. Taylor
C.E. Till
J.J. Vaitekunas
R.W. Weeks
R.A. Winans
H. Wiedersich
P. S. Wong
ANL Patent Dept.
ANL Contract Files
ANL Libraries
TIS Files (3)

External:

DOE-TIC, for distribution per UC-111 and UC-115 (45)

DOE-CH
D.T. Goldman
F. Herbaty

ACUSTICA E SONICA S/C/L, P.O. Box 12.946, Sao Paulo, Brazil
Professor L.X. Nepomuceno

ADVANCED MATERIALS & PROCESSES, Rt. 87, Metals Park, OH 44073
Laurel M. Sheppard

AFWAL/MLLP, Wright-Patterson AFB, OH 45433-6533
Allan Katz
Joseph Moyzis
Robert Ruh
Dale E. Chimenti

AFSOR/NE, Bolling AFB, Washington, D.C. 20332-6448
Liselotte J. Schioler

AIR PRODUCTS AND CHEMICALS, INC., Box 538, Allentown, PA 18105
Ken Baumert

ALCAN INTERNATIONAL LIMITED, Kingston Research & Development Center
P.O. Box 8400, Kingston, Ontario, CANADA K7L 4Z4
Gregory Hayes

ALCOA TECHNICAL CENTER, Alcoa Center, PA 15069
Thomas Drumwright
Martin Jones
John Weyand
Neal Dando

ALLIED SIGNAL AEROSPACE CO., Garrett Ceramic Components Div., 19800 Van Ness Avenue, Torrance, CA 90509
J.R. Pollinger
Hun C. Yeh

APTECH ENGINEERING SERVICES, 1257 Elko Drive, Sunnyvale, CA 94089
G.R. Egan

ARMY MATERIALS TECHNOLOGY LABORATORY, Arsenal St., SLCMT-OMM

ARMY MATERIALS TECHNOLOGY LABORATORY, Arsenal St., SLCMT-OMM
Watertown, MA 02172
Al Broz James Marzik

ATOMIC ENERGY OF CANADA, Chalk River Nuclear Labs.
Ontario, KOJ 1JO CANADA
Stuart MacEwen Barbara Sawicka

BABCOCK & WILCOX RESEARCH CENTER, P. O. Box 785, Lynchburg, VA 24505
William Long Tom Powers

BORG-WARNER CORPORATION, Wolf-Algonquin Roads, Des Plaines, IL 60018
Vance Brown Al Karvelas
Donatus Tijunelis

BRITISH PETROLEUM COMPANY, Chertsey Road, Sudbury-on-Thames
Middlesex TW167LN ENGLAND
C. I. Nicholls

CERAMATEC, INC., 163 West 1700 South, Salt Lake City, UT 84115
Raymond Cutler David W. Richerson

CHISHOLM INSTITUTE OF TECHNOLOGY 900 Dandenong Road
Caulfield East, Victoria, AUSTRALIA 3145
John R. Davis

COLUMBIA SCIENTIFIC INDUSTRIES CORP., 11950 Jollyville Rd.,
P.O. Box 203190, Austin, TX 78720
Dr. S. Piorek

COORS PORCELAIN COMPANY, Golden, CO 80401
J.E. Knight Dennis Kruetzer
Dave Wirth

CORNING GLASS WORKS SP-FR-51 Sullivan Park, Corning, NY 14831
David C. Larsen R. Patricia Morris Paul A. Russell

CUMMINS ENGINE COMPANY, Box 3005, Mail Code 50183
Columbus, IN 47202-3005
Thomas M. Yonushonis

DARPA, Materials Science Division, Defense Sciences Office
1400 Wilson Blvd., Arlington, VA 22209-2308
Kay Hardman-Rhyne

DeBEERS INDUSTRIAL DIAMOND DIVISION, P.O. Box 916, Johannesburg 2000,
Republic of South Africa
Mrs. A. Nolan

E.I. duPONT COMPANY Engineering Physics Lab, Wilmington, DE 19898
John D. Anthony, Jr. Thomas W. Harding

ELECTRIC POWER RESEARCH INSTITUTE, 3412 Hillview Ave.
P. O. Box 10412, Palo Alto, CA 94303
Steve Gehl Wate T. Bakker

FERRO, 7500 E. Pleasant Valley Road., Independence, OH 44131
Alan G. King

FORD MOTOR CO., P.O. Box 2053, S-3039 Scientific Res. Labs.
Dearborn, MI 48121
Lee Feldkamp Keith Caruthers

GARRETT TURBINE ENGINE COMPANY, 111 S. 34th St.,
P.O. Box 5217, Phoenix, AZ 85010
Janet Minter Vicki E. Panhuise

GAS RESEARCH INSTITUTE, 8600 W. Bryn Mawr Ave., Chicago, IL 60631
Matt Schriener Max Klein

GENERAL ELECTRIC COMPANY, M.D. 45, Aircraft Engine Division,
Cincinnati, OH 45215
D. Copley B. Nightingale

GENERAL MOTORS CORPORATION Allison Div. P.O. Box 420
Indianapolis, IN 46206
Pramod Khandelwal

GTE LABORATORIES, INC. 40 Sylvan Road, Waltham, MA 02254
Gus Bandyopadhyay William Koenigsberg
Arvid E. Pasto Les Bowen

GTE/WESGO, 509 Calle DeSoto, San Clemente, CA 92672
Harry Kerr

HUGHES AIRCRAFT, Electro-Optical, 2175 Park Place, P.O. Box 902
El Segundo, CA 92045
J. E. Almanza

IDAHO NATIONAL ENGINEERING LABORATORY EG&G Idaho, Inc.
P.O. Box 1625, Idaho Falls, ID 83415
J. B. Walter

INDUSTRIAL MATERIAL RESEARCH INSTITUTE OF CANADA, 75 Boulevard,
De Mortagne, Boucherville, Quebec, CANADA J4B 5K5
Jean Bussiere Jean-Pierre Monchalin

INDUSTRIAL QUALITY INC., P.O. Box 2397, Gaithersburg, MD 20879-0397
Harry Berger

IOWA STATE UNIVERSITY/Electrical Engineering Department, Ames, Iowa 50011
Bill Lord

IOWA STATE UNIVERSITY/APPLIED SCI. CTR., Ames Lab, Ames, Iowa 50011
D. O. Thompson

ISRAEL ATOMIC ENERGY COMMISSION, Soreq Nuclear Research Center,
70600 Yavne, Israel
Dr. A. Gayer

JOHNS HOPKINS UNIVERSITY, Center for Nondestructive Evaluation,
Maryland Hall, Baltimore, MD 21218
John Murphy Robert E. Green, Jr.

LANXIDE CORPORATION. Tralee Industrial Park, Newark, DE 19711
J. G. Weinstein C. R. Kennedy

LAWRENCE LIVERMORE NATIONAL LABORATORY, P. O. Box 808, Livermore, CA 94550
Ronald Streit

LENOX CHINA, Tilton Road, Pomona, NJ 08240
John T. Jones

LOS ALAMOS NATIONAL LABORATORY, P.O. Box 1663, Los Alamos, NM 87545
F. D. Gac David Stupin

McMASTER UNIVERSITY, Hamilton, Ontario, CANADA L8S 4L7
P. S. Nicholson

MARTIN MARIETTA LABS, 1450 S. Rolling Rd., Baltimore, MD 21227
Boro B. Djordjevic

MASSACHUSETTS INSTITUTE OF TECHNOLOGY, Dept. of Materials and Components, Rm. 12-009, Cambridge, MA 02139
H. K. Brown

MINNESOTA MINING AND MANUFACTURING (3M), New Products Division
3M Center, St. Paul, MN 55144
Jane S. Copes

MOBIL RESEARCH AND DEVELOPMENT CORP., Dallas Research Laboratory
13777 Midway Rd., Dallas, TX 75244-4312
Dr. M.E. Coles

NASA/GODDARD SPACE FLIGHT CENTER, Ceramics Section, Greenbelt, MD 20771
Thomas Heslin

NASA LEWIS RESEARCH CENTER, Mail Stop 6-1, 2100 Brookpark Rd.
Cleveland, OH 44135
George Baaklini Stan Klima Alex Vary

NATIONAL BUREAU OF STANDARDS, Ceramics Division, Bldg. 420
Gaithersburg, MD 20899
Sandy J. Dapkunas Edwin R. Fuller, Jr.
Tom Yolken G. V. Blessing

NATIONAL BUREAU OF STANDARDS, Fracture and Deformation Div.,
325 S. Broadway, Boulder, CO 80303
A. V. Clark

NAVAL AIR PROPULSION CENTER, Systems Technology Div., Science and Technology, Trenton, NJ 08628
Joseph W. Glatz

NAVAL SURFACE WEAPONS CENTER, Code R34, Silver Spring, MD 20903-5000
Cliff Anderson

NONDESTRUCTIVE TESTING CENTER, AERE HARWELL, Bldg. 149, Oxfordshire, England OX11 ORA
W. N. Reynolds

NORTON COMPANY, Advanced Ceramics, Goddard Road, Northboro, MA 05132-1545
Kamal E. Amin W.S. Coblenz
P. Tewari

OAK RIDGE NATIONAL LABORATORY P. O. Box 2008, Oak Ridge, TN
D. Ray Johnson (Bldg. 4515, MS 066)/37831-6066
R. R. Judkins (Bldg. 4500S, MS 153)/37831-6153

OFFICE OF NAVAL RESEARCH, Code 431
800 N. Quincy St., Arlington, VA 22217
Robert C. Pohanka (Code 431)
Yapa Rajapakse (Code 1132-SM), Mechanics Division

OFFICE OF TECHNOLOGY ASSESSMENT, Energy and Materials Program, U.S. Congress, Washington, DC 20510
Greg Eyring

OHIO STATE UNIVERSITY, Ceramic Engineering Department
2041 College Rd., Columbus, OH 43210
Dennis Readey, Dept. Chairman

PANAMETRICS, INC., 221 Crescent St., Waltham, MA 02154
Larry Lynnworth

PENNSYLVANIA STATE UNIVERSITY, University Park, PA 16802
Clay O. Ruud, Materials Research Laboratory
Richard E. Tressler, Ceramic Science & Engineering Dept.

RUTGERS UNIVERSITY, Center for Ceramic Research, Box 909
Piscataway, NJ 08854
John B. Wachtman, Jr.

SANDIA NATIONAL LABORATORY, Div. 7551, Albuquerque, NM 87185
K. R. Thompson

SCIENTIFIC MEASUREMENT SYSTEMS, 2201 Donley Drive, Austin, TX 78758
Hunter Ellinger

SHELL DEVELOPMENT COMPANY, P. O. BOX 1380, Houston, TX 77251
Lynton W.R. Dicks

SKEGA AB S-934, 02 Ersmark, SWEDEN
Erik Ostman
Sture Persson

SOHIO ENGINEERED MATERIALS CO., Niagara Falls R & D Center,
P. O. Box 832, Niagara Falls, NY 14302
Wolfgang D. G. Boecker M. Srinivasan

SOHIO ENGINEERED MATERIALS, Research & Development Center,
4440 Warrensville Center Rd., Cleveland, OH 44128-2837
William Friedman Phil Engler
P. K. Hunt

SOLVAY TECHNOLOGIES, INC., 609 Fifth Ave., New York, NY 10017
George Gerliczy

SOUTHWEST RESEARCH INSTITUTE, P. O. Box 28510, San Antonio, TX 78284
Amos E. Holt

SRI INTERNATIONAL, 333 Ravenswood Ave., Menlo Park, CA 94025
David J. Rowcliffe

STANFORD UNIVERSITY, Ginzton Laboratory, Stanford, CA 94305
Gordon Kino

SVENSKA, SWEDISH INSTITUTE FOR SILICATE RESEARCH, Box 5403 S-402,
29 Goteborg SWEDEN
Brita Nyberg

TEXAS A&M UNIVERSITY, Dept. of Mechanical Eng., College Station,
TX 77843
Don E. Bray Christian Burger

TEXAS RESEARCH INSTITUTE, 9063 Bee Caves Rd., Austin, TX 78733-6201
George Matzkanin

TOHOKU UNIVERSITY, Dept. of Elec. Engineering, Sendai 980, JAPAN
Jun-ichi Kushibiki

UNITED TECHNOLOGIES & RESEARCH CENTER, East Hartford, CT 06108
Harry Ringermacher Richard Williams

UNIVERSITAT DES SAARLANDES, Inst. fur Zerstorungsfreie Profverfahren,
Bau 37, D-6600 Saarbrucken, West Germany
Prof. Dr. Paul Holler

UNIVERSITY OF HOUSTON, Mechanical Eng. Dept., Houston, TX 77004
Kamel Salama

UNIVERSITY OF ILLINOIS-URBANA, Dept. of General Engineering,
Urbana, IL 61801
Henrique Reis

UNIVERSITY OF MASSACHUSETTS, Mechanical Engineering Dept.
Amherst, MA 01003
John E. Ritter, Jr.

UNIVERSITY OF OXFORD, Metallurgy Dept./Parks Rd.
Oxford OX13PH, ENGLAND
Andrew Briggs

UNIVERSITY OF WASHINGTON, Materials Science & Engineering Dept.
Roberts Hall, FB-10, Seattle, Washington 98115
Richard C. Bradt

U. S. ARMY TACOM, AMSTA-RGRT, Warren, MI 48397-5000
Thomas M. Sebestyen Douglas Rose

U. S. BUREAU OF MINES, 2401 I Street, N.W., Washington, D.C. 20241
Murray A. Schwartz

U. S. DOE IDAHO OPERATIONS OFFICE, Energy Programs Branch
550 2nd St., Idaho Falls, ID 83401
W. H. Thielbahr, Chief

U. S. DOE OAK RIDGE OPERATIONS, Federal Building Room 2039
Oak Ridge, TN 37830
E. E. Hoffman

U. S. DOE OFFICE OF ADVANCED ENERGY CONVERSION, FE-22, GTN,
Washington, D.C. 20545
John W. Fairbanks

U. S. DOE OFFICE OF ENERGY CONSERVATION, Forrestal Bldg., CE-142,
1000 Independence Ave., Washington, D.C. 20585
J. J. Eberhardt S. M. Wolf Scott Richlen

U.S. DOE OFFICE OF FOSSIL ENERGY [GTN], Technical Coordination/
Advanced Research, Washington, DC 20545
J. P. Carr D. J. Beecy

U. S. DOE OFFICE OF BASIC ENERGY SCIENCES, MATERIAL SCIENCES
DIVISION, ER-131 GTN, Washington, D.C. 20545
Robert J. Gottschall

U.S. DOE OFFICE OF ENERGY CONSERVATION, TRANSPORTATION SYSTEMS
DIVISION, Forrestal Bldg., Washington, DC 20585
Melvin H. Chiogioji Albert A. Chesnes
Richard T. Alpaugh E. E. Ecklund
R. B. Schulz

W. R. GRACE & CO., 7379 Route 32,, Columbus, MD 21044
Roy W. Rice

Materials and Components Technology Division Review Committee:

Dr. Peter Alexander, Director/Engineering, Combustion Engineering, 400 West Avenue, Rochester, NY 14611
Dr. Leslie J. Jardine, Program Manager, Bechtel National, Inc., 45 Fremont St., 11/B33, San Francisco, CA 94105
Dr. Stanley J. Green, Dir., Steam Generator Project Office, EPRI, 3412 Hillview Ave., Palo Alto, CA 94105
Dr. Robert A. Greenkorn, Vice President/Research, Purdue University, Hovde Hall, Room 222, West Lafayette, IN 47907
Prof. Che-Yu Li, Materials Science & Engineering/Bard Hall, Cornell University, Ithaca, NY 14853
Dr. Roger E. Scholl, URS/John Blume & Assoc., 150 Fourth Street, Sixth Floor, San Francisco, CA 94103
Dr. Paul G. Shewmon, Professor & Chairman, Metallurgical Engineering, Ohio State University, Columbus, OH 43210
Dr. Richard E. Smith, Manager, Maintenance & Repair Applications Division, EPRI NDE Center, P.O. Box 217097, Charlotte, NC 28221